

# No increase is detected and ~~modeled~~ modelled for the seasonal cycle amplitude of $\delta^{13}\text{C}$ of atmospheric carbon dioxide

Fortunat Joos<sup>1,2</sup>, Sebastian Lienert<sup>1,2</sup>, and Sönke Zaehle<sup>3</sup>

<sup>1</sup>Climate and Environmental Physics, University of Bern, Bern Switzerland

<sup>2</sup>Oeschger Centre for Climate Change Research, University of Bern, Bern, Switzerland

<sup>3</sup>Max Planck Institute for Biogeochemistry, P.O. Box 600164, Hans-Knöll-Str. 10, 07745 Jena, Germany

**Correspondence:** Fortunat Joos (fortunat.joos@unibe.ch)

**Abstract.** Measurements of the seasonal cycle of  $\delta^{13}\text{C}$  (~~of atmospheric~~  $\text{CO}_2$  ( $\delta^{13}\text{C}_a$ )) provide information on the global carbon cycle and the regulation of carbon and water fluxes by leaf stomatal openings on ecosystem and decadal scales. Land biosphere carbon exchange is the primary driver of  $\delta^{13}\text{C}(\text{CO}_2)_a$  seasonality in the Northern Hemisphere. We use isotope-enabled simulations of the Bern3D-LPX Earth System Model of Intermediate Complexity and fossil fuel emission estimates with a model of atmospheric transport to simulate ~~local~~ atmospheric  $\delta^{13}\text{C}(\text{CO}_2)_a$  at globally distributed monitoring sites. Unlike the observed growth of the seasonal amplitude of  $\text{CO}_2$  at northern sites, no significant temporal trend in the seasonal amplitude of  $\delta^{13}\text{C}(\text{CO}_2)_a$  ~~is~~ was detected at most sites, consistent with the insignificant model trends. Comparing the preindustrial ~~and modern (1700) and modern (1982-2012)~~ periods, the ~~modeled~~ modelled small amplitude changes at northern sites are linked to the near-equal increase of background atmospheric  $\text{CO}_2$  and the seasonal signal of the net atmosphere-land  $\delta^{13}\text{C}$  flux in the northern extratropical region, with no long-term temporal changes in the isotopic fractionation ~~by  $\text{C}_3$  in these ecosystems~~ dominated by  $\text{C}_3$  plants. The good data-model agreement in the seasonal amplitude of  $\delta^{13}\text{C}(\text{CO}_2)_a$  and its decadal trend provides implicit support for the regulation of stomatal conductance by  ~~$\text{C}_3$~~   $\text{C}_3$  plants towards intrinsic water use efficiency to grow proportionally to atmospheric  $\text{CO}_2$  over recent decades. Disequilibrium fluxes contribute little to the seasonal amplitude of the net land isotope flux north of  $40^\circ\text{N}$  but contribute near-equally to the isotopic flux associated with growing season net carbon uptake in tropical and Southern Hemisphere ecosystems, pointing to the importance of monitoring  $\delta^{13}\text{C}(\text{CO}_2)_a$  over these ecosystems. We propose to apply seasonally-resolved  $\delta^{13}\text{C}(\text{CO}_2)$  ~~observations as a novel~~ observations as an additional constraint for land biosphere models and underlying processes for improved projections of the anthropogenic carbon sink.

*Copyright statement.* TEXT

## 1 Introduction

The seasonal variations in the carbon exchange fluxes between the atmosphere and the surface cause a seasonal cycle in atmospheric  $\text{CO}_2$  ( $C_a$ ) (Keeling et al., 1996; Graven et al., 2013; Masarie et al., 2014) and its stable isotopic signature ( $\delta^{13}\text{C}_a$ ) (Keeling, 1960; Keeling et al., 1984, 1989, 2005; GLOBALVIEW-CO2C13, 2009), with  $\delta^{13}\text{C}$  defined by  $\delta^{13}\text{C} = [R_{\text{sample}}/R_{\text{std}} - 1] \times$

1000, where  $R_{\text{sample}}$  and  $R_{\text{std}}$  are the  $^{13}\text{C}/^{12}\text{C}$  abundance ratios of the sample and the carbonate standard "PDB" (0.0112372), respectively (Craig, 1957). Observations of the atmospheric seasonal cycles in background tropospheric air provide large-scale information on the carbon fluxes between the atmosphere, ocean, and land (Heimann et al., 1989, 1998) and constraints for models used to project atmospheric  $\text{CO}_2$  and global warming.

The additional information of  $\delta^{13}\text{C}$  data in comparison to carbon data stems from differences in fractionation for different carbon fluxes. Carbon isotopic fractionation describes the preferential transfer of light  $^{12}\text{C}$  compared to heavier  $^{13}\text{C}$ . The degree of fractionation is different for the different physical, chemical, and biological processes (Mook, 1986) causing differences in the isotopic composition of carbon reservoirs and fluxes. The seasonal  $\delta^{13}\text{C}_a$  variations result from the combination of carbon and isotopic fluxes from fossil fuel burning, land use, and the exchange of the atmosphere with the ocean, and land biosphere. Comparing results of carbon isotope-enabled models with observations of  $\delta^{13}\text{C}_a$  is useful to assess whether the mix of carbon and isotopic sink and source fluxes is represented consistently in comparison with the observations.  $\delta^{13}\text{C}_a$  observations offer, therefore, a benchmark for evaluating and improving earth system models.

Fractionation is particularly large during the assimilation of  $\text{CO}_2$  from the atmosphere by plants following the  $\text{C}_3$  photosynthesis pathway which are responsible for most of the global productivity (Still et al., 2003). Importantly, changes in isotopic fractionation by  $\text{C}_3$  plants are indicative of changes in stomatal conductance, regulating the leaf-internal  $\text{CO}_2$  mixing-ratio, and thus photosynthesis (Farquhar, 1989; Saurer and Voelker, 2022; Cernusak and Ubierna, 2022). Photosynthesis, the associated water loss, and evaporative cooling are key characteristics of ecosystem function that are central to the cycles of carbon, nitrogen, water, and energy (Keenan et al., 2013; Knauer et al., 2017) and for the land sink of anthropogenic carbon. Acquisition of  $\text{CO}_2$  for photosynthesis is accompanied by the loss of water through the stomatal pores that govern, by their conductance, the diffusion of these two gases between the leaf interior and the atmosphere. A key question is how ecosystems adjust their overall conductance and, thereby, co-regulate carbon uptake and plant growth, and water loss and evaporative cooling under rising atmospheric  $\text{CO}_2$ , growing nitrogen inputs to ecosystems, and increasing water vapor deficits under global warming. Many studies, relying on multi-decadal to century-scale tree-ring  $\delta^{13}\text{C}$  records and free air  $\text{CO}_2$  enrichment (FACE) experiments, suggest small changes in isotopic fractionation and intrinsic water use efficiency, the ratio of assimilation to conductance, to grow roughly proportionally with atmospheric  $\text{CO}_2$  (Voelker et al., 2016; Saurer et al., 2014; Kauwe et al., 2013; Peñuelas et al., 2011; Keller et al., 2017; Frank et al., 2015). In contrast, Battipaglia et al. (2013) and Keenan et al. (2013) suggest a scenario where conductance and the flows of carbon and water are downregulated under increasing  $\text{CO}_2$ . Keeling et al. (2017), analyzing decadal-scale change in seasonally detrended  $\delta^{13}\text{C}_a$  and the annual atmospheric budgets of carbon and  $^{13}\text{C}$ , find a decrease in isotopic fractionation of global mean net primary production; the change is attributed to changes in fractionation associated with mesophyll conductance and photorespiration of  $\text{C}_3$  plants and intrinsic water use efficiency is inferred to grow proportionally with  $\text{CO}_2$ . Conflicting results for 20th-century changes in fractionation and intrinsic water use efficiency are also found in global land biosphere models (Keller et al., 2017). Upscaling of results from site studies to large scales is challenging. It remains to be assessed whether a scenario with small long-term changes in fractionation of  $\text{C}_3$  plants is compatible with atmospheric  $\delta^{13}\text{C}_a$  observations representing carbon fluxes over large regions.

The observational records from globally distributed monitoring sites (Keeling et al., 1996; Graven et al., 2013; Masarie et al., 2014) demonstrate a significant growth trend in the seasonal cycle amplitude ( $SA$ ) of  $C_a$  (Keeling et al., 1996; Graven et al., 2013) (Bacastow et al., 1985; Keeling et al., 1996; Graven et al., 2013; Barlow et al., 2015; Piao et al., 2018), driven by changes in the seasonality of net land carbon uptake (Graven et al., 2013; Forkel et al., 2016). The observed seasonal cycle and amplitude growth of  $C_a$  are widely used to evaluate carbon cycle models and system understanding by transporting fluxes from terrestrial, oceanic, and fossil sources with a model of atmospheric transport to obtain local  $C_a$  anomalies (Heimann et al., 1998; Dargaville et al., 2002; Scholze et al., 2008; Peng et al., 2015; Lienert and Joos, 2018). Studies address the role of different climatic drivers and terrestrial carbon cycle processes such as drought, land use, warming, productivity, and soil respiration (Heimann et al., 1989, 1998; Graven et al., 2013; Forkel et al., 2016; Ito et al., 2016; Bastos et al., 2019; Wang et al., 2020) and surface-to-atmosphere C fluxes (e.g. Peylin et al. (2013) Peylin et al. 2013).  $SA(C_a)$  and their temporal trends at different monitoring sites are used for constraining an ensemble of land biosphere model simulations (Lienert and Joos, 2018).

Comparable studies, analyzing the temporal trends in  $SA(\delta^{13}C_a)$  and the seasonal cycle of  $\delta^{13}C_a$ , are ~~to our knowledge, lacking scarce~~. While seasonally-resolved atmospheric  $\delta^{13}C_a$  measurements are available (GLOBALVIEW-CO2C13, 2009; Keeling et al., 2001), these seasonally-resolved records are yet to be fully utilized in the context of processed-based carbon cycle models. Heimann et al. (1989) simulated the spatiotemporal distribution of  $\delta^{13}C_a$  and  $C_a$  with an atmospheric transport model using estimates of net primary productivity and heterotrophic respiration based on satellite data and surface temperature and prescribed surface ocean  $CO_2$ , demonstrating the dominant role of land biosphere fluxes for northern hemisphere seasonality and finding relevant signals from the ocean and land in the southern hemisphere. van der Velde et al. (2018) applied their Carbon Tracker Data Assimilation System for  $CO_2$  and  $^{13}CO_2$  by varying the net exchange fluxes of  $CO_2$  and  $^{13}CO_2$  in ocean and terrestrial biosphere models and propagating the fluxes through an atmospheric transport model to solve for weekly adjustments to fluxes and isotopic terrestrial discrimination minimizing differences between observed and estimated mole fractions. They identified a decrease in stomatal conductance on a continent-wide scale during a severe drought. Ballantyne et al. (2011) applied an analytical regression approach to analyze the differences in isotopic signatures between northern hemisphere site data versus free troposphere background data from Niwot Ridge to infer seasonal variations in the source signature of the net atmosphere-land biosphere flux and to evaluate models of stomatal conductance. Observations of  $\delta^{13}C_a$  seasonal cycles ~~have been were~~ used to investigate isotopic fractionation (Ballantyne et al., 2010) and trends in the phenology of northern terrestrial ecosystems (Gonsamo et al., 2017), but to our knowledge have not been used ~~as a benchmark for model performance in combination with an atmospheric transport model and~~ for analyzing trends in  $SA(\delta^{13}C_a)$  globally.

This study addresses the following main questions:

1. Is the seasonal cycle of  $\delta^{13}C_a$  observed at a network of globally distributed sites well represented in model simulations?  
How large are the contributions of ocean, land, and fossil fuel fluxes to  $\delta^{13}C_a$  seasonality?
2. What are the temporal trends in  $SA(\delta^{13}C_a)$  in the observational records and are the ~~modeled~~ modelled trends in  $SA(\delta^{13}C_a)$  consistent with the observed trends?

90 3. What are the different drivers of  $SA(\delta^{13}C_a)$  versus  $SA(C_a)$  and of their temporal trends? Is a model scenario with intrinsic water use efficiency growing proportional with ~~atmospheric  $CO_2$~~   $C_a$  consistent with  $\delta^{13}C_a$  seasonality data?

We simulate atmospheric  $\delta^{13}C_a$  and  $C_a$  at 19 globally distributed sites using the matrix representation of an atmospheric transport model and net atmosphere-to-surface fluxes of  $CO_2$  and  $\delta^{13}(CO_2)$  from an Earth System Model of Intermediate Complexity (EMIC) alongside gridded fossil fuel emission estimates and changes in land use and the distribution of  ~~$C_3$  and  $C_4$~~   $C_3$  and  $C_4$  crops. We compare model results to observations and analyze trends in  $SA(\delta^{13}C_a)$  using the records of the Scripps  $CO_2$  program (Keeling et al., 2001) and the Cooperative Global Atmospheric Data Integration Project (2013) product. ~~We demonstrate for the first time that the observations at the globally distributed sites show no significant trends in the seasonal cycle amplitude of  $\delta^{13}C_a$ , consistent with our model chain, but surprising in view of the large trend in the seasonal amplitude of  $CO_2$ .~~ We discuss the implications of our results for changes in the fractionation by  ~~$C_3$~~   $C_3$  plants, their stomatal controls, and associated carbon and water fluxes. We develop a theoretical framework to explain the trends in  $SA(\delta^{13}C_a)$  and decompose net carbon and isotope land biosphere fluxes into underlying component fluxes and changes in carbon fluxes and fractionation. The framework could serve future studies, e.g., studies applying an ensemble of different models for multi-model evaluation and more robust conclusions in comparison to using a single model chain.

100

## 2 Methods

### 105 2.1 Bern3D-LPX Earth System Model of Intermediate Complexity

Spatially-resolved surface-to-atmosphere  $CO_2$  and  $^{13}CO_2$  fluxes are simulated with the ~~EMIC~~ Bern3D-LPX Earth System Model of Intermediate Complexity. Here, the ocean-atmosphere model Bern3D (Jeltsch-Thömmes and Joos, 2020; Battaglia and Joos, 2018; Ritz et al., 2011) is coupled to the Dynamic Global Vegetation Model (DGVM) framework of the Land surface Processes and eXchanges (LPX) model, LPX-Bern v1.4 (Lienert and Joos, 2018). The Bern3D model features a ~~41x~~ 40 horizontal ocean resolution (about  ~~$9^{\circ} \times 4.5^{\circ}$~~   $4.5^{\circ}$ ) with 32 depth layers, coupled to a single-layer energy-moisture balance atmosphere (Ritz et al., 2011). In Bern3D, carbon and its isotopes are implemented as tracers with fractionation for air-sea and sea-air gas exchange, aquatic chemistry, and the production of organic material and  $CaCO_3$  as a function of surface ocean temperature, aqueous  $CO_2$ , and the speciation of ~~DIC~~ dissolved inorganic carbon as described by ~~Jeltsch-Thömmes and Joos (2023)~~ Jeltsch-Thömmes and Joos (2023). LPX-Bern simulates the coupled cycling of carbon, nitrogen, and water (Xu-Ri and Prentice, 2008; Wania et al., 2009a, b; Stocker et al., 2014) and vegetation dynamics using plant functional types (Sitch et al., 2003). It is here run on a  $3.75^{\circ} \times 2.5^{\circ}$  resolution. Grid cells are subdivided into different land use classes (mineral soil, wetlands, crop, pasture, urban). Carbon isotopes were added (Scholze et al., 2003) using a photosynthetic fractionation scheme (Lloyd and Farquhar, 1994) and without further isotopic fractionation during the transfer through vegetation, litter, soil, and product pools. The scheme neglects fractionation by boundary layer transport and ternary effects associated with the interaction of  $CO_2$ , water, and air (Farquhar and Cernusak, 2012) and fractionation by "dark" day respiration is set to zero, while fractionation by the following terms is explicitly considered: stomatal conductance (with a scaling factor of 4.4‰), dissolution and liquid

110

120

[transport \(1.8‰\), carboxylation \(27.5‰\), and photorespiration \(8‰ and the CO<sub>2</sub> compensation point that would occur in the absence of dark respiration,  \$\Gamma^\*\$ , is increasing with temperature\)](#) (Lloyd and Farquhar, 1994). The signature of respired carbon reflects the signature of carbon assimilated at previous times; the lag times between assimilation and respiration are dictated  
125 by the turnover time scales of the various pools, depending on temperature and soil moisture. Land carbon and isotope fluxes respond to altered climate, which influences, for example, photosynthesis through temperature and water limitation, fire frequency, and autotrophic and heterotrophic respiration rates, to increasing  $\text{CO}_2\text{C}_a$ , which stimulates photosynthesis and affects water use efficiency ("CO<sub>2</sub> fertilization"), and to land use (Strassmann et al., 2008), which causes, for example, transfer of tree carbon to the atmosphere, litter, and product pools after deforestation and shifts from natural vegetation to ~~C3 and C4~~ [C<sub>3</sub> and C<sub>4</sub>](#) crops and pasture, and to altered nitrogen deposition and nitrogen fertilizer addition on managed land alleviating nitrogen  
130 limitation.

Bern3D and LPX-Bern were spun up individually, followed by a 500-year coupled spinup to pre-industrial equilibrium (1700 CE; 276.3 ppm, -6.27 ‰). A transient simulation,  $E_{\text{standard}}$ , from 1700 to 2020 is driven by annual fossil carbon emissions (including the contribution from cement production) (Friedlingstein et al., 2020), net land use area changes (Hurtt et al., 2020),  
135 and non-CO<sub>2</sub> radiative forcing.  $\delta^{13}\text{C}$  of the fossil fuel emissions follows Andres et al. (2017) for 1751-2014 and set to the value for 1751 before. For 2014-2020, signatures of major source categories (coal, oil, gas, cement) are assumed constant and combined with the emission sources from Friedlingstein et al. (2020), following the approach of Andres et al. (2000). Here, we explicitly distinguish land use classes for ~~C3 and C4~~ [C<sub>3</sub> and C<sub>4</sub>](#) crops and prescribe their extent, and net land use area changes, based on [LUH2 the Land-Use Harmonization 2 dataset](#) (Hurtt et al., 2020). Nitrogen deposition and nitrogen fertilization are  
140 taken from the [NMIP-project N<sub>2</sub>O Model Intercomparison Project](#) (Tian et al., 2018). Nitrogen (N) is a limiting nutrient in LPX and plant growth is downregulated under N-stress, which tends to reduce plant growth and plant growth responses to rising  $\text{CO}_2\text{C}_a$  compared to a model with absent N cycling. The ~~NCEP/NCAR~~ monthly wind stress climatology [from the NCEP/NCAR Reanalysis produced by the National Centers for Environmental Prediction \(NCEP\) and the National Center for Atmospheric Research \(NCAR\)](#) (Kalnay et al., 1996) is prescribed to the ocean. ~~Monthly climate fields from CRU-TS4~~ [Climatic Research Unit \(CRU\) Time-Series \(TS\) version 4.05 of high-resolution gridded data of month-by-month variation in climate \(CRU TS4.05\)](#) (Harris et al., 2020) are used for the land model. For 1700-1900 and the spinup, the climate of 1901-1931 is recycled. A control simulation, ~~termed~~  $E_{\text{control}}$ , without anthropogenic CO<sub>2</sub> emissions, and absent radiative forcing from non-CO<sub>2</sub> ~~agents species~~ (e.g., from CH<sub>4</sub>, N<sub>2</sub>O, ozone), land use, nitrogen deposition, and nitrogen fertilization at 1700 level, as well as recycling 1901-1931 land climate provides a baseline. ~~Atmospheric CO<sub>2</sub> C<sub>a</sub>~~ and  $\delta^{13}\text{C}_a$  evolve freely in all simulations  
145 presented and remain at their preindustrial values in  $E_{\text{control}}$ .

## 2.2 Atmospheric Transport Model TM3 and the seasonal cycles of $\text{CO}_2\text{C}_a$ and $\delta^{13}\text{C}_a$

We employ the transport matrices of the ~~TM3 atmospheric global atmospheric tracer model TM3, a three-dimensional~~ transport model (Heimann and Körner, 2003; Kaminski et al., 1998; Schürmann et al., 2016) to translate surface-atmosphere fluxes from Bern3D-LPX and fossil emissions into  $\text{CO}_2(\text{C}_a)$  and  $\delta^{13}\text{C}(\text{CO}_2)(\delta^{13}\text{C}_a)$  anomalies at 19 measurement sites across the globe.  
155 Before transport, the fluxes are remapped to the TM3 72x48 grid ( $5^\circ \times 3.75^\circ \times 3.75^\circ$ ). Here, the matrices span from 1982 to

2012 and are only available if there is also a CO<sub>2</sub> measurement available at the corresponding site. Each matrix represents the sensitivity of the local atmospheric concentration for a given month to the local surface fluxes of the previous period, spanning up to 48 months. The transport model is initialized with equal C<sub>a</sub> and δ<sup>13</sup>C<sub>a</sub> at all sites.

For <sup>13</sup>C, the signature-weighted net atmosphere-to-surface flux is:

$$160 \quad \delta^{13} f_{as,net}(\mathbf{x}, t) = f_{as,net}(\mathbf{x}, t) \cdot \delta^{13} C_{as,net}(\mathbf{x}, t). \quad (1)$$

δ<sup>13</sup>f<sub>as,net</sub> is in units of mol permil m<sup>-2</sup> yr<sup>-1</sup>.  $\mathbf{x}$  indicates location and  $t$  time at the monthly and spatial (5° × 3.75°) resolution of TM3. The net carbon fluxes (f<sub>as,net</sub>; mol m<sup>-2</sup> yr<sup>-1</sup>), their signatures (δ<sup>13</sup>C<sub>as,net</sub>), and, therefore, δ<sup>13</sup>f<sub>as,net</sub>, are readily available for fossil emissions, including cement production (Andres et al., 2009b, a). Bern3D-LPX simulates two-way exchange of CO<sub>2</sub> and <sup>13</sup>CO<sub>2</sub> from and to the ocean and land surface. Net transfer rates are determined by the difference of these gross  
165 fluxes to yield atmosphere-to-surface net fluxes f<sub>as,net</sub> and δ<sup>13</sup>f<sub>as,net</sub> of Bern3D-LPX.

The matrices are applied with f<sub>as,net</sub> to compute anomalies in C<sub>a</sub> and with δ<sup>13</sup>f<sub>as,net</sub> to compute anomalies in <sup>13</sup>CO<sub>2</sub>. We get δ<sup>13</sup>C<sub>a</sub> from <sup>13</sup>CO<sub>2</sub>/C<sub>a</sub>. This method of transporting signature-weighted net fluxes was chosen instead of separately transporting <sup>13</sup>CO<sub>2</sub> and <sup>12</sup>CO<sub>2</sub>. Both approaches were tested and showed very similar results, except for numerical issues in months having very small local <sup>12</sup>CO<sub>2</sub> anomalies for the second approach.

170 Ocean, land, and fossil fluxes from the standard simulation are transported separately to quantify the contributions of these individual components to the seasonal variations in C<sub>a</sub> and δ<sup>13</sup>C<sub>a</sub>. For E<sub>control</sub>, fossil fuel fluxes are not transported, consistent with the model setup. A limitation is that transport matrices are only available for the period 1982 to 2012, limiting the analysis period and direct model-data comparison to three decades only.

### 2.3 Site data

175 ~~Observations~~ Background CO<sub>2</sub> from 19 monitoring sites are, for which transport matrices are available, is used for comparison with simulated C<sub>a</sub> and δ<sup>13</sup>C<sub>a</sub> and to determine observation-based trends in their SA. The Cooperative Global Atmospheric Data Integration Project (2013) product is used for C<sub>a</sub>. For δ<sup>13</sup>C<sub>a</sub>, the records of the Scripps CO<sub>2</sub> program (Keeling et al., 2001) for Alert, Mauna Loa, and the South Pole from monthly-averaged flask data are used. These records span a longer period than the available transport matrices. For the remaining 16 sites, the shorter (1994 to 2009) records of GLOBALVIEW-CO2C13  
180 (2009) are used. In the main manuscript, we focus on 3 out of the 19 available transport sites: Alert (82.5°N, Canada), Mauna Loa (19.5°N, Hawaii), and South Pole (90°S, Antarctica). Results for the other sites are shown in the supplementary and Table 1. The Scripps and GLOBALVIEW-CO2C13 data are on a slightly different scale (Lueker et al., 2020); this does not affect our analysis of seasonal anomalies. The δ<sup>13</sup>C<sub>a</sub> records of GLOBALVIEW-CO2C13 (2009) span order of a decade and are, therefore, not used for trend detection, although we evaluated trends from the simulations for the GLOBALVIEW sites (Table 2; excluding Key Biscayne). We require at least 10 monthly values for a year to be included in the linear regression.  
185

Additional δ<sup>13</sup>C<sub>a</sub> monthly flask data from the Scripps CO<sub>2</sub> program (Keeling et al., 2001) are used for analyzing temporal trends in the SA(δ<sup>13</sup>C<sub>a</sub>). We focus on eight sites with more than twenty years of data: Alert (ALT, 82°N), Point Barrow (PTB, 71°N, La Jolla (LJO, 33°N), Mauna Loa Observatory (MLO, 20°N), Cape Kumukahi (KUM, 20°N), Christmas Island

(CHR, 2°N), Samoa (SAM, 14°S), and South Pole (SPO, 90°S). The ~~records from Kermadec Island (KER, 29°S) and Baring~~  
 190 ~~Head, New Zealand (NZD, 41°S) extend over more than 20 years, but have often missing monthly values.~~ data are provided  
as (i) monthly samples, (ii) a fit to these monthly samples, and (iii) the monthly samples but missing values replaced with  
fitted values. We also used the original, non-gap-filled data and years with at least 9, 10, or 11 monthly values per year in the  
regression.

### 3 The influence of carbon and isotope fluxes on the seasonal cycles of $\text{CO}_2$ and $\delta^{13}\text{CO}_2$ : a conceptual 195 framework

We develop a simplified conceptual framework to qualitatively explore the influence of carbon and isotope fluxes on the seasonal cycles of  $C_a$  and  $\delta^{13}C_a$ . For illustration, the atmosphere is considered to be well mixed in this section; the atmospheric transport operator is linear and the findings may qualitatively also apply to spatially-resolved fluxes. The budgets for the atmospheric inventories of carbon and  $^{13}\text{C}$  are approximated (Tans et al., 1993):

$$200 \quad \frac{d}{dt} N_a = -F_{as,net} \quad (2)$$

$$\frac{d}{dt} (N_a \cdot \delta^{13}C_a) = \left( \frac{d}{dt} N_a \right) \cdot \delta^{13}C_a + N_a \cdot \left( \frac{d}{dt} \delta^{13}C_a \right) = -F_{as,net} \cdot \overline{\delta^{13}C_{as,net}} \quad (3)$$

$N_a$  and  $N_a \cdot \delta^{13}C_a$  are the atmospheric inventories of carbon and (approximately) of  $^{13}\text{C}$  (in mol permil).  $F_{as,net}$  and  $F_{as,net} \cdot \overline{\delta^{13}C_{as,net}}$  are the globally integrated net atmosphere-to-surface carbon and  $^{13}\text{C}$  flux;  $\overline{\delta^{13}C_{as,net}}$  is the signature of  
 205 the global net carbon flux. We set  $N_a = c \cdot C_a$ , where  $c$  is a unit conversion factor. Solving Eqs. 2 and 3 for the change in  $C_a$  and  $\delta^{13}C_a$  yields:

$$\frac{d}{dt} C_a = \frac{-1}{c} \cdot F_{as,net} \quad (4)$$

$$\frac{d}{dt} \delta^{13}C_a = \frac{-1}{c \cdot C_a} \cdot \delta^{13} F_{as,net}^* \quad (5)$$

210 with  $\delta^{13} F_{as,net}^*$  being the global integral of

$$\delta^{13} f_{as,net}^* = f_{as,net} \cdot (\delta^{13}C_{as,net} - \delta^{13}C_a) \quad (6)$$

The superscript \* indicates that the  $^{13}\text{C}$  fluxes (e.g., in units of mol permil  $\text{yr}^{-1} \text{m}^{-2}$  for  $\delta^{13} f_{as,net}^*$ ) are referenced to the atmospheric signature. Eq. 6 corresponds to Eq. 1 for the net atmosphere-to-surface isotopic flux but is now referenced to the atmospheric signature instead of the signature of 0 permil of the Vienna Pee Dee Belemnite standard as in Eq. 1. In this way, a  
 215 positive (negative) flux causes a ~~positive~~ ~~(negative)~~ ~~negative~~ (positive) change in  $\delta^{13}C_a$ .

Eqs. 4 and 5 are readily integrated over the growing season from the intraannual maximum to the minimum (subscripts max, min) in  $C_a$  and the corresponding beginning,  $t_{beg}$ , and end time,  $t_{end}$ , of the growing season to get the seasonal cycle amplitude ( $SA$ ) for the two tracers and (cumulative) net fluxes (see Appendix A for calculation of  $SA$  for a flux):

$$\underbrace{C_{a,max} - C_{a,min}}_{SA(C_a)} = \frac{1}{c} \underbrace{\int_{t_{beg}}^{t_{end}} F_{as,net}(t) dt}_{SA(F_{as,net})} \quad (7)$$

220

$$\underbrace{\delta^{13}C_{a,max} - \delta^{13}C_{a,min}}_{SA(\delta^{13}C_a)} = \frac{-1}{c \cdot C_a} \underbrace{\int_{t_{beg}}^{t_{end}} \delta^{13}F_{as,net}^*(t) dt}_{SA(\delta^{13}F_{as,net}^*)} \quad (8)$$

Eqs. 5 and 8 provide important insight. First, changes in  $\delta^{13}C_a$  and its seasonal cycle are driven by  $\delta^{13}F_{as,net}^*$ ; seasonal changes in  $C_a$ , the denominator in Eq. 5, are small compared to  $C_a$  and  $C_a$  considered constant within a given year (the error associated with this approximation is less than 3%). Second, the background  $\text{CO}_2$  mixing-ratiomole fraction,  $C_a$ , modulates the magnitude of the  $\delta^{13}C_a$  seasonal cycle.  $SA(\delta^{13}C_a)$  would be larger under low preindustrial  $\text{CO}_2$ - $C_a$  than under modern  $\text{CO}_2$ - $C_a$  for equal seasonal variations in  $\delta^{13}F_{as,net}^*$ . Correspondingly,  $SA(\delta^{13}C_a)$  does not change over time as long as relative changes in  $SA(\delta^{13}F_{as,net}^*)$  and in  $\text{CO}_2$ - $C_a$  are equal. Equations 7 and 8 were derived for a globally well mixed atmosphere and global fluxes, but analogously also apply for the tracer seasonality at individual sites with the integral on the right-hand side of Eqs. 7 and 8 representing the integral of (transport-weighted) fluxes over the region influencing tracer seasonality at the site. We recall that the above equations and conclusions were derived by assuming a well-mixed atmosphere, while in reality spatial flux patterns and transport and their changes influence seasonal cycles at individual atmospheric sites. Further, the start and end of the growing season are assumed to coincide with the switch in the sign of the isotopic flux; this is the case in our model for zonally integrated fluxes. These seasonal fluxes will be presented in section 3.34.3. Equations 2 to 8 are for illustrating the influence of carbon and carbon isotope fluxes on the seasonal cycles of  $\text{CO}_2$ - $C_a$  and  $\delta^{13}\text{CO}_2$ - $C_a$ ; they were not used for calculating numerical results.

235

The notation and sign convention introduced above are applied in this manuscript. In brief,  $f_{i,j}$  defines a one-way flux from the source reservoir  $i$  to the receiving reservoir  $j$  and is positive. The isotopic signature of this flux is  $\delta^{13}C_{i,j}$ . The net flux from reservoir  $i$  to reservoir  $j$  is  $f_{i,j,net}$  and is the difference between the corresponding one-way fluxes, e.g.,  $f_{i,j,net} = f_{i,j} - f_{j,i}$ .  $f_{i,j,net}$  is positive if the net flux results in the transfer of mass from  $i$  to  $j$ .

## 240 4 Results

### 4.1 Seasonal cycles of atmosphere-surface fluxes, $C_a$ , and $\delta^{13}C_a$

The ~~model simulates~~ Bern3D-LPX model simulates (E<sub>standard</sub>) large seasonal variations in the net land biosphere-atmosphere exchange of  $\text{CO}_2$  and  $^{13}\text{CO}_2$ , whereas seasonal variations in ocean-atmosphere fluxes are much smaller (Fig. 1). ~~The seasonality~~



**Table 1.** The seasonal cycle amplitude of  $C_a$  and  $\delta^{13}C_a$  from the standard simulation ( $E_{\text{standard}}$ ) and observations (Obs) for 19 monitoring sites and the period 1982-2012. The increase over the industrial period is estimated from the difference between the standard simulation and the preindustrial control ( $100 \cdot (E_{\text{standard}} - E_{\text{control}}) / E_{\text{control}}$ ).

Site	Seasonal Cycle Amplitude of $C_a$			Seasonal Cycle Amplitude of $\delta^{13}C_a$		
	Standard Model [ppm]	Observed [ppm]	Increase $\frac{\text{StdMod}-\text{Obs}}{\text{Obs}}$ [%]	Standard Model [permil]	Observed [permil]	Increase $\frac{\text{StdMod}-\text{Obs}}{\text{Obs}}$ [%]
Alert, Nunavut, Canada (82°N)	17.26 ± 0.84	14.82 ± 0.75	2.44	0.719 ± 0.035	0.750 ± 0.042	-0.030
Barrow, Alaska, US (71°N)	20.10 ± 1.06	15.79 ± 0.75	4.31	0.899 ± 0.041	0.822 ± 0.030	0.077
Ocean Station M, Norw. (66°N)	17.73 ± 1.14	14.77 ± 0.93	2.96	0.763 ± 0.051	0.752 ± 0.028	0.010
Cold Bay, Alaska, US (55°N)	14.83 ± 0.80	15.91 ± 1.00	-1.08	0.657 ± 0.032	0.847 ± 0.029	-0.190
Shemya Island, Alaska, US (53°N)	14.63 ± 0.88	17.03 ± 0.98	-2.40	0.655 ± 0.038	0.926 ± 0.029	-0.271
Mace Head, Ireland (53°N)	14.65 ± 1.15	13.64 ± 1.74	1.01	0.618 ± 0.046	0.726 ± 0.039	-0.107
Terceira Island, Portugal (39°N)	11.70 ± 0.86	9.39 ± 1.18	2.31	0.497 ± 0.028	0.517 ± 0.036	-0.020
Key Biscayne, Florida, US (26°N)	8.97 ± 0.78	8.17 ± 2.31	0.79	0.350 ± 0.031	0.405 ± 0.040	-0.055
Mauna Loa, Hawaii, US (20°N)	8.33 ± 0.30	6.51 ± 0.24	1.82	0.328 ± 0.013	0.339 ± 0.028	-0.010
Cape Kumukahi, Hawaii (20°N)	9.07 ± 0.39	7.96 ± 0.53	1.11	0.358 ± 0.017	0.423 ± 0.028	-0.065
Mariana Islands, Guam (13°N)	6.36 ± 0.41	6.11 ± 0.72	0.26	0.254 ± 0.019	0.312 ± 0.022	-0.058
Ragged Point, Barbados (13°N)	8.00 ± 0.39	7.10 ± 0.45	0.89	0.306 ± 0.017	0.332 ± 0.027	-0.026
Christmas Island, Kiribati (2°N)	4.68 ± 0.35	2.95 ± 0.38	1.74	0.161 ± 0.016	0.129 ± 0.018	0.033
<del>Ascension Island, UK</del> ( <del>8°S</del> )	<del>3.17-3.52</del> ± 0.41	<del>1.81-2.57</del> ± 0.41	<del>1.37</del>	<del>0.134-0.145</del> ± 0.012-0.015	<del>0.073-0.113</del> ± 0.016-0.021	<del>0.061-0.032</del>
<del>Mabe Island, Seychelles</del> ( <del>5°S</del> )	<del>3.52-3.17</del> ± 0.41	<del>2.57-1.81</del> ± 0.41	<del>0.95</del>	<del>0.145-0.134</del> ± 0.015-0.012	<del>0.113-0.073</del> ± 0.021-0.016	<del>0.032-0.061</del>
Tutuila, American Samoa (14°S)	1.29 ± 0.28	0.89 ± 0.30	0.40	0.044 ± 0.007	0.020 ± 0.009	0.024
Palmer Station, Antarctica (65°S)	2.60 ± 0.25	1.41 ± 0.19	1.20	0.107 ± 0.008	0.037 ± 0.008	0.070
Halley Station, Antarctica (76°S)	2.57 ± 0.15	1.09 ± 0.16	1.48	0.103 ± 0.005	0.027 ± 0.007	0.076
South Pole, Antarctica (90°S)	2.06 ± 0.16	1.09 ± 0.11	0.97	0.094 ± 0.004	0.033 ± 0.015	0.061

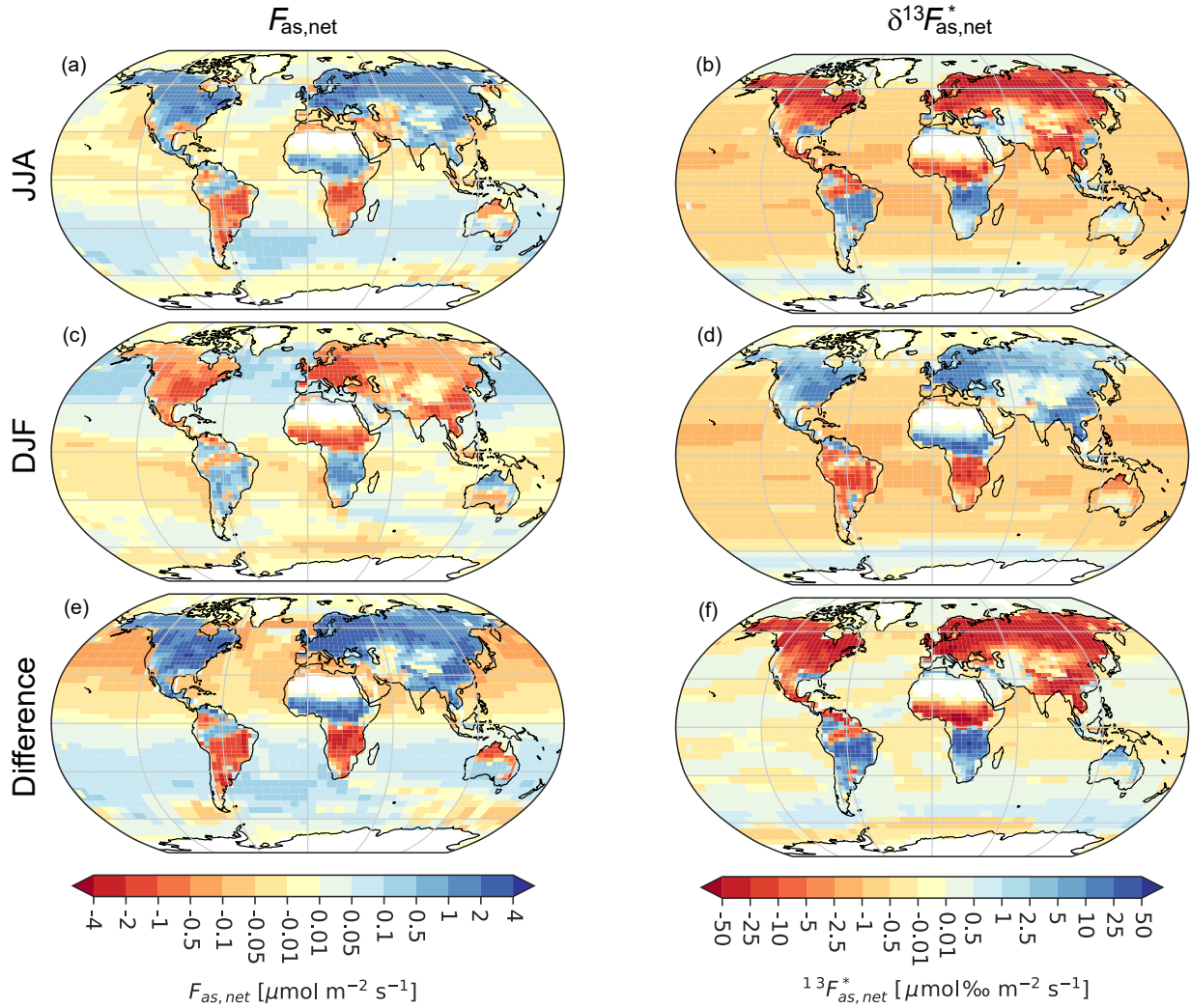


**Figure 1.** Net seasonal atmosphere-to-surface fluxes. Fluxes are for (a,c,e) carbon and (b,d,f) the  $\delta^{13}\text{C}$ -weighted carbon flux,  $\delta^{13}f_{as,net}^*$  (see section 3) from the standard simulation ( $E_{\text{standard}}$ ) and averaged over 1982-2012 for (a,b) June, July, August (JJA), (c,d) December, January, February (DJF), and (e,f) JJA minus DJF. Note non-linear color bars with blue colors in panels a to d indicating a lowering in atmospheric  $\text{CO}_2$  and  $\delta^{13}\text{C}$ , respectively.

of the Bern3D-LPX carbon fluxes. This seasonality is broadly consistent with estimates of regional air-land carbon flux seasonality from an atmospheric inversion (Gurney et al., 2004) and air-sea flux seasonality from surface ocean pCO<sub>2</sub> observations (Fay et al., 2021) (Landschützer et al., 2014; Takahashi et al., 2009; Fay et al., 2021), except in the Southern Ocean. The and in the northern subpolar gyres. The LPX land biosphere model shows the expected uptake of isotopically depleted carbon, resulting in positive  $f_{as,net}$  and negative  $\delta^{13}f_{as,net}^*$  during the summer and vice versa in winter. On a separate note, the nominal signature of the net carbon flux,  $\delta^{13}C_{as,net}$ , may be diagnosed by dividing  $\delta^{13}f_{as,net}$  by  $f_{as,net}$ .  $\delta^{13}C_{as,net}$  can become very large for small  $f_{as,net}$ , is hard to interpret, and not used in our approach.

The Bern3D ocean model shows a negative  $\delta^{13}f_{as,net}^*$  in low and mid-latitudes, small modern fluxes in the northern subpolar gyres, and a positive flux in the Southern Ocean in both seasons (Fig. 1). These modern Bern3D fluxes are driven by the atmosphere-ocean isotopic disequilibrium, here defined as the isotopic signature of the atmosphere-to-surface carbon flux minus the signature of the surface-to-atmosphere flux ( $\delta_{dis,as}$ ; Eq. A2), with a negative  $\delta_{dis,as}$  in low and mid-latitudes, a small modern disequilibrium in northern high latitudes, and a positive  $\delta_{dis,as}$  south of 50°S, consistent with observations (Menviel et al., 2015; Quay et al., 2017; Becker et al., 2018).

The preindustrial air-sea isotopic disequilibrium ( $\delta_{dis,as}$ ; see Appendix A) and  $\delta^{13}f_{as,net}^*$  are negative in low- and mid-latitude and positive in high-latitude ocean regions (not shown), mainly driven by the temperature dependency of isotopic fractionation during air-sea exchange and the cycling of marine biological matter (see Fig. 1 of Menviel et al. (2015) for a comparison of comparing Bern3D and LOVECLIM results for the atmosphere-ocean disequilibrium  $\delta_{dis,as}$ ). Fossil fuel emissions cause a negative flux perturbation worldwide, shifting the net isotopic fluxes to more negative values over the industrial period.

Figure 2 compares the mean seasonal cycles of  $C_a$  and  $\delta^{13}C_a$  from the standard run  $E_{standard}$  with measurements from 1982 (Alert: 1985) to 2012 at three sites, and with factorial simulations, where the fluxes of land (green dashed line), the ocean (blue dashed line), and fossil fuel emissions (brown dashed lines) were considered individually (See Table 1 and Supplementary Information, Fig. S1 and S2 for additional sites). For the Northern Hemisphere (NH) sites of Alert (top panels) and Mauna Loa (middle panels), the seasonal variations are dominated by the terrestrial biosphere fluxes, with minor contributions from ocean fluxes and fossil fuel emissions. Note that in contrast to the seasonality of  $C_a$ , the seasonality of  $\delta^{13}C_a$  does not linearly decompose into the contributions of land, ocean, and fossil fuel emissions.

Both the timing and amplitude of the observed seasonal cycle of  $C_a$  and  $\delta^{13}C_a$  are captured reasonably well by the standard simulation  $E_{standard}$  (Fig. 2). The simulated  $SA(C_a)$  and its interannual variability (IAV) are overestimated compared to observations at Alert ( $17.3 \pm 0.84$  ppm vs  $14.8 \pm 0.75$ ) and Mauna Loa ( $8.3 \pm 0.30$  ppm vs  $6.5 \pm 0.24$  ppm).  $SA(\delta^{13}C_a)$  matches the observations (ALT:  $0.72 \pm 0.035$  ‰ vs  $0.75 \pm 0.042$  ‰; MLO:  $0.34 \pm 0.013$  ‰ vs  $0.33 \pm 0.028$ ). Good model-data agreement in the phasing of the seasonal cycle of  $C_a$  relative to  $\delta^{13}C_a$  is demonstrated for Alert in panel (c), where monthly anomalies in  $\delta^{13}C_a$  are plotted versus anomalies in  $C_a$ . Both observation and model show hysteresis throughout the year, with the loop rotating clockwise. At Mauna Loa, the rotation direction of the hysteresis loop is clockwise in the simulation and anticlockwise in the observation (panel (f)), but. Still, the observed hysteresis is small with offsets of less than 0.03 ‰. The hysteresis arises as the ratio between the rate of change in  $\delta^{13}C_a$  versus the rate of change in  $C_a$  varies over the year (Keeling et al., 1989;

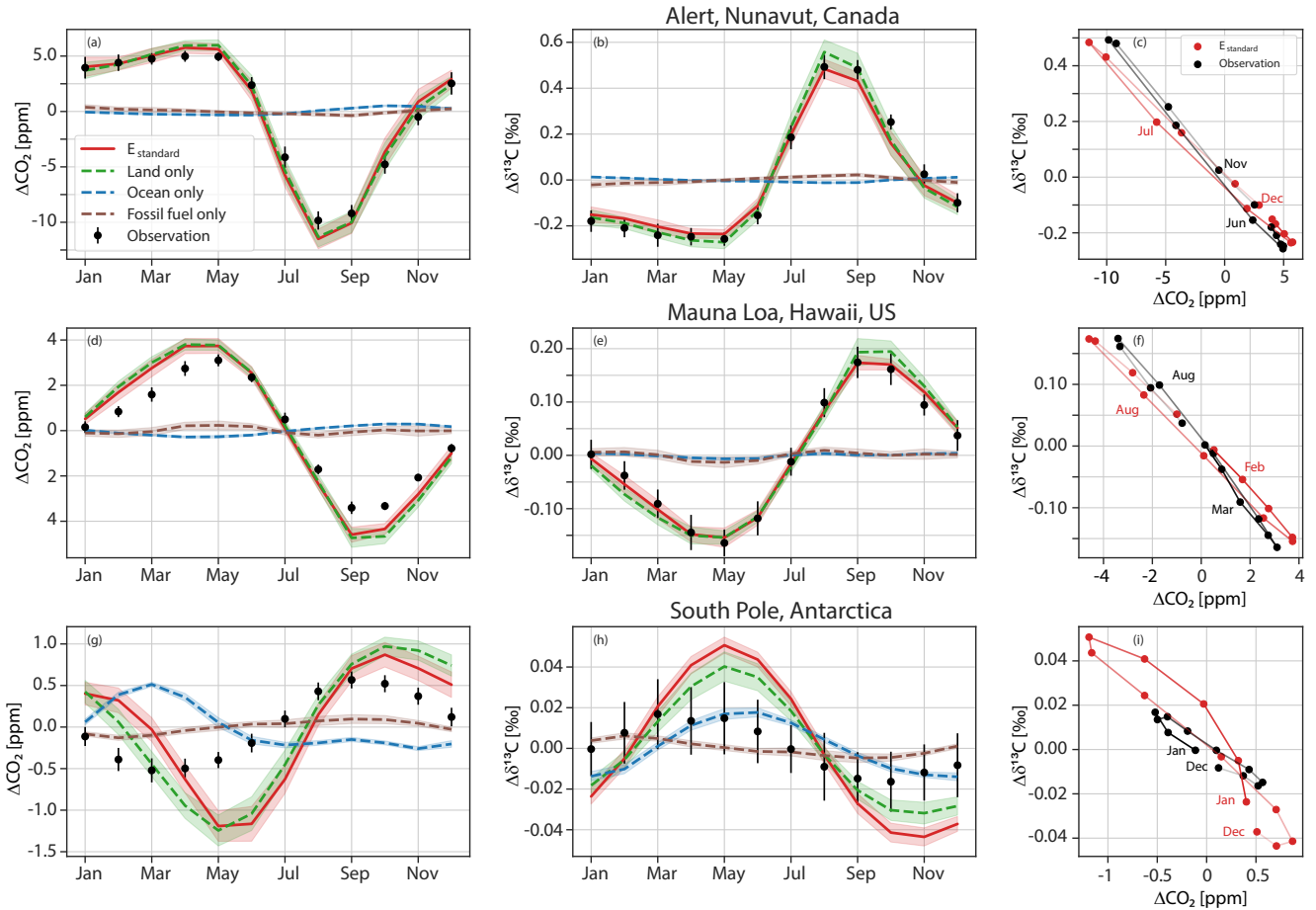


**Figure 2.** The simulated (red) seasonal cycle of atmospheric  $\epsilon\text{CO}_2\text{-C}_a$  (left (a,d,g)) and its signature  $\delta^{13}\text{C}_a$  (middle (b,e,h)), compared to observations (black dots). In the rightmost panels (c,f,i) the seasonal anomalies ( $\Delta$ ) of  $\epsilon\text{CO}_2\text{-C}_a$  are plotted against those of  $\delta^{13}\text{C}_a$ , with lines connecting the monthly values (dots) fading from January to December. Results are for Alert, northern Canada (a,b,c), Mauna Loa, Hawaii (d,e,f), and the South Pole (g,h,i). Simulated values are from transporting in TM3 net fluxes of the Bern3D-LPX [standard](#)  $E_{\text{standard}}$  simulation from all (red,  $E_{\text{standard}}$ ), terrestrial (green, dashed), oceanic (blue, dashed), and fossil sources (brown, dashed). The observational and model anomalies are computed from monthly values between 1982 and 2012 if both the measurements and transport matrices are available. Error bars and shading correspond to the standard deviation from the interannual variability of monthly values.

Heimann et al., 1989). This non-linearity in the atmospheric tracer relationship originates from seasonally varying transport in  
280 combination with spatially and temporally varying relationships of atmosphere-surface  $\delta^{13}\text{C}$  to  $\text{CO}_2$  flux. For example, the isotopic signature of the growing season net atmosphere-to-land carbon flux  $\delta^{13}\text{C}_{al,net}$  is  $-13.4\text{‰}$  for the northern high-latitude region ( $>40^\circ\text{N}$ ), but only  $-10.7\text{‰}$  for the region  $10^\circ\text{N}$ - $40^\circ\text{N}$  and the signal observed at any measurement site results from varying contributions from these and other latitudinal bounds given intraannually varying winds and hence transport.

Results for the South Pole are different than for the NH sites (Fig. 2 (g,h,j)). Neither the timing nor the amplitude of  $C_a$   
285  $(2.1\pm 0.16\text{ ppm simulated vs } 1.1\pm 0.11\text{ ppm observed})$  and  $\delta^{13}\text{C}_a$   $(0.094\pm 0.004\text{‰ vs } 0.033\pm 0.015\text{‰})$  agree with observations.  $SA(C_a)$  and  $SA(\delta^{13}\text{C}_a)$  at the South Pole are observed to be 14 and 23 times smaller than at Alert, respectively. The absolute data-model mismatches are therefore not as drastic as the relative mismatches. The disagreement between simulation and observational estimates is also apparent when considering the scatter plot in panel (i). The model shows a complex hysteresis relationship, whereas the observation displays a clockwise loop.

290 The remote Antarctic sites (South Pole, Palmer, and Halley) show an expected relatively larger dependence on the ocean, but the terrestrial contribution still dominates in the model (Figs. 2, S1, and S2). The  $C_a$  seasonal cycle resulting from atmosphere-ocean flux is shifted by up to six months compared to observations at the South Pole and the other two Antarctic sites (Palmer, Halley; blue lines versus black dots in Fig. S1), pointing to biases in the Bern3D ocean flux. ~~The Bern3D ocean fluxes and their seasonality are broadly comparable to observational estimates over large parts of the ocean (Landschützer et al., 2014; Takahashi et al., 2009), with ocean  $\text{CO}_2$  outgassing in the tropics and uptake in the mid-latitudes during winter (Fig. 1). However, observation-based~~  
295 Observation-based analyses indicate stronger ocean  $\text{CO}_2$  uptake in summer than in winter in the Southern Ocean (Jin et al., 2024; Long et al., 2021; Fay et al., 2021) and the northern subpolar gyres, in contrast to results from Bern3D (Fig. 1) and more complex ocean models (Hauck and Völker, 2015) and several Earth System Models from CMIP5 (Majkut et al., 2014) and CMIP6 (Joos et al., 2023). The simulated amplitude and phasing of the  $\delta^{13}\text{C}_a$  seasonal cycle resulting from the ocean are  
300 broadly in line with observations at the Antarctic sites (Fig. S2). The air-sea isotopic disequilibrium is large in the Southern Ocean and the two-way, air-sea and sea-air, exchange fluxes yield a substantial net isotopic flux, even under low net carbon flux. Temperature-dependent fractionation is higher in winter than summer and the air-sea gas exchange piston velocity, and, in turn, the isotope fluxes are larger under high winds in winter than in summer in the model Southern Ocean, consistent with the observed seasonal phasing of  $\delta^{13}\text{C}_a$  at the Antarctic sites. Errors in ~~modeled~~ modelled Southern Ocean fluxes are expected  
305 to have a minor impact on simulated  $SA(C_a)$  and  $SA(\delta^{13}\text{C}_a)$  at NH sites, where the influence of land fluxes dominates by far (Fig. 2, S1, S2).

Considering all extratropical Northern Hemisphere sites, model-data mismatches are less than 30% for  $SA(C_a)$  and  $SA(\delta^{13}\text{C}_a)$   
and their root mean square errors (RMSE) are 2.6 ppm and 0.14 permil, respectively. For the tropical and SH sites, large relative data-model deviations of up to 140% for  $SA(C_a)$  and up to 290% for  $SA(\delta^{13}\text{C}_a)$  are evident, although absolute deviations are  
310 less than 1.8 ppm and 0.18 permil and the corresponding RMSEs are 1.2 ppm and 0.05 permil (Table 1).

Interannual variability in simulated  $SA(\delta^{13}\text{C}_a)$  compares reasonably well with observations at sites in the NH subtropics and extratropics (average of the  $1-\sigma$  standard ~~deviation~~ deviation of 12 sites:  $0.031\text{‰}$  in  $E_{standard}$  versus  $0.031\text{‰}$  in observations) and in the tropics and SH ( $0.009$  vs.  $0.013\text{‰}$ ) (Table 1). ~~Similar~~ A similar agreement between simulated and observation-

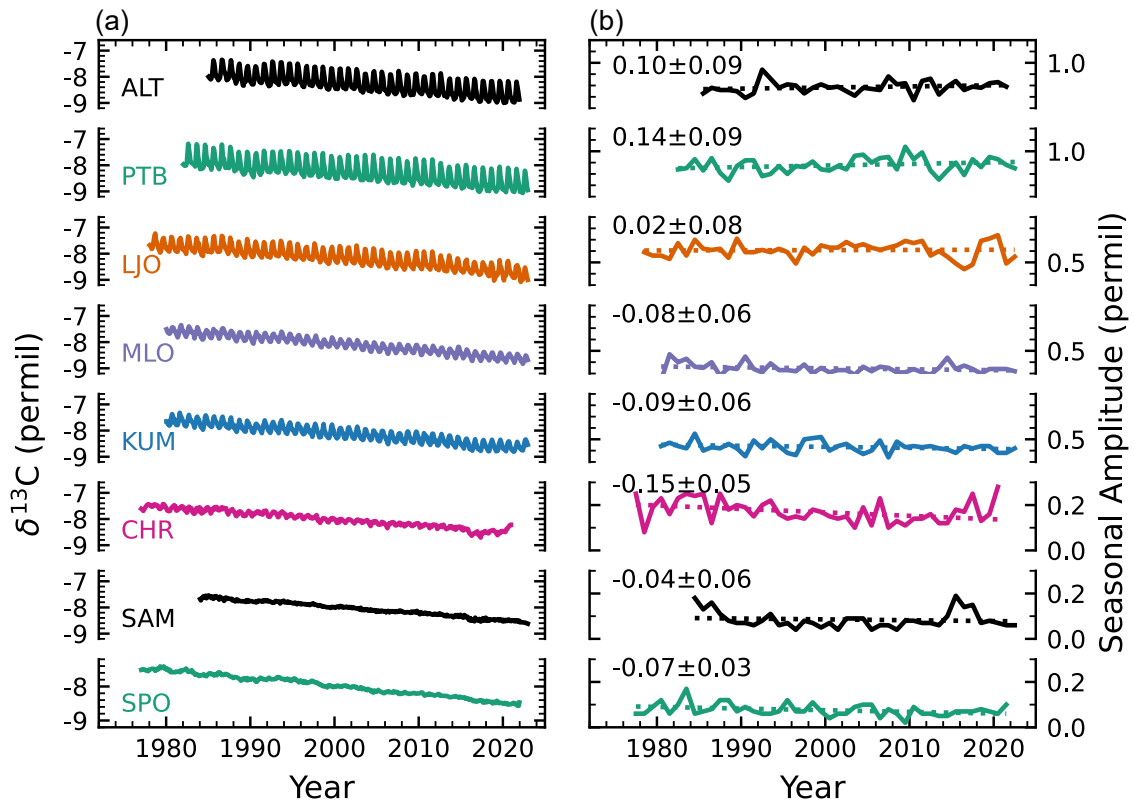


**Figure 3.** Temporal evolution of  $\delta^{13}C_a$  (left) and its seasonal amplitude (right) from data of the Scripps network (Keeling et al., 2001). Gap-filled data provided by Scripps are used for the eight sites. The slope and its standard error from a linear regression through the seasonal amplitude data (dotted) are given in permil/century. Trends are not different from zero based on a two-sided t-test and a significance level of 5%, except at Christmas Island (CHR) and the South Pole (SPO). [Sites are ordered according to latitude \(Alert \(ALT, 82°N\), Point Barrow \(PTB, 71°N, La Jolla \(LJO, 33°N\), Mauna Loa Observatory \(MLO, 20°N\), Cape Kumukahi \(KUM, 20°N\), Christmas Island \(CHR, 2°N\), Samoa \(SAM, 14°S\), and South Pole \(SPO, 90°S\).\)](#)

315 derived IAV holds for  $SA(C_a)$  (NH extratropics: 0.75 vs 0.96 ppm; tropics and SH: 0.29 vs 0.30). This further-suggests that the variability in the seasonal amplitude of the underlying-carbon and isotope fluxes is reasonably represented by LPX-Bern. The correct simulation of variability can be challenging and van der Velde et al. (2013) report too low interannual variability in the annually-integrated isotopic disequilibrium flux for their model.

#### 4.2 Temporal trends in the seasonal cycle amplitude of $\delta^{13}C_a$ and $C_a$

**Table 2.** Temporal trends in the seasonal cycle amplitude of  $C_a$  and  $\delta^{13}C_a$  from the standard simulation ( $E_{\text{standard}}$ ) and observations for 19 monitoring sites from 1982-2012. Observational data of  $\text{CO}_2-C_a$  are from the [GLOBALVIEW-CO2](#) product and fitted for the period 1982-2012, while the data for  $\delta^{13}C_a$  are from [SCRIPPS-Scripps](#) and fitted as shown in Fig. 3. The seasonal cycle amplitude of a given year is only computed if at least 10 monthly values are available. Number of years included in the trend calculation for  $SA(C_a)$  and model-based  $SA(\delta^{13}C_a)$  are given in parentheses. The observed trend for  $C_a$  is affected by anomalous values at Key Biscayne and is not included. Over the period 1982-2012, significant trends (two-sided t-test at 5% significance) are only found for Alert, Barrow, Ocean Station M, and Mahe Island for observed  $C_a$ , for Mariana Islands, Mahe Island, Palmer, Halley, and South Pole for simulated  $C_a$ , and Ascension, Mahe Island, and South Pole for simulated  $\delta^{13}C_a$ . The decadal-scale trends are given per century for better readability.

Site	Trend in Seasonal Cycle Amplitude		$\delta^{13}C_a$ [permil/century]
	$C_a$ [ppm/century]	Observed	
Alert, Nunavut, Canada (82°N)	Observed: $6.5 \pm 2.3$	Observed: $0.1 \pm 0.09$	$0.02 \pm 0.13$ (25)
Barrow, Alaska, US (71°N)	$9.5 \pm 1.9$	$0.14 \pm 0.09$	$-0.09 \pm 0.15$ (26)
Ocean Station M, Norw. (66°N)	$7.2 \pm 3.1$	$7.7 \pm 3.9$	$0.02 \pm 0.17$ (25)
Cold Bay, Alaska, US (55°N)	$1.3 \pm 4.4$	$5.2 \pm 4.4$	$0.10 \pm 0.20$ (25)
Shemya Island, Alaska, US (53°N)	$-0.5 \pm 5.3$	$-0.4 \pm 4.9$	$-0.04 \pm 0.22$ (21)
Mace Head, Ireland (53°N)	$-9.6 \pm 14.0$	$-5.6 \pm 4.3$	$-0.27 \pm 0.24$ (15)
Terceira Island, Portugal (39°N)	$-1.5 \pm 6.6$	$5.7 \pm 3.7$	$0.10 \pm 0.17$ (14)
Key Biscayne, Florida, US (26°N)		$1.5 \pm 1.7$	$0.03 \pm 0.07$ (25)
Mauna Loa, Hawaii, US (20°N)	$-1.6 \pm 1.0$	$0.6 \pm 1.4$	$-0.07 \pm 0.05$ (26)
Cape Kumukahi, Hawaii (20°N)	$-2.1 \pm 2.0$	$2.2 \pm 1.6$	$-0.01 \pm 0.06$ (26)
Mariana Islands, Guam (13°N)	$-2.6 \pm 4.8$	$4.1 \pm 1.5$	$0.08 \pm 0.05$ (23)
Ragged Point, Barbados (13°N)	$-2.1 \pm 2.1$	$-0.3 \pm 1.7$	$-0.06 \pm 0.07$ (18)
Christmas Island, Kiribati (2°N)	$-2.4 \pm 1.8$	$-1.9 \pm 1.6$	$-0.13 \pm 0.07$ (19)
<a href="#">Ascension Island, UK</a> (7.6°Mahe Island, Seychelles (5°S))	$2.7-3.7 \pm 1.8-1.4$	$-0.6-6.4 \pm 1.4-2.3$	$-0.15-0.30 \pm 0.05(-25)$ $0.07(13)$
<a href="#">Mahe Island, Seychelles</a> (5°Ascension Island, UK (7.6°S))	$3.7-2.7 \pm 1.4-1.8$	$6.4-0.6 \pm 2.3-1.4$	$0.30-0.15 \pm 0.07(-13)$ $0.05(25)$
Tutuila, American Samoa (14°S)	$2.2 \pm 1.3$	$-0.5 \pm 0.9$	$-0.04 \pm 0.02$ (26)
Palmer Station, Antarctica (65°S)	$-0.4 \pm 0.9$	$2.4 \pm 1.1$	$0.04 \pm 0.04$ (23)
Halley Station, Antarctica (76°S)	$0.1 \pm 1.8$	$2.9 \pm 1.1$	$0.03 \pm 0.04$ (17)
South Pole, Antarctica (90°S)	$0.7 \pm 0.8$	$2.8 \pm 0.7$	$0.06 \pm 0.03$ (26)

Temporal trends in  $SA(\delta^{13}C_a)$  from the Scripps gap-filled data are not statistically different from zero, except at the tropical site Christmas Island and the South Pole (Fig. 3). Averaging the trends across all 8 sites yields  $-0.0038 \pm 0.026$  permil/century (mean  $\pm$  1 sdv of mean) and averaging the trends for the extratropical sites ALT, PTB, and LJO yields  $+0.09 \pm 0.06$  permil/century, with both averaged trends not statistically different from zero. The trend for the NH extratropical sites translates into a change in  $SA(\delta^{13}C_a)$  of around  $5 \pm 3\%$  over the 40-year observational period. Detection of trends in  $SA(\delta^{13}C_a)$  may be hampered by interannual-to-decadal variability, short record lengths, and a small  $SA(\delta^{13}C_a)$  in comparison to measurement uncertainty and variability as typical at Southern Hemisphere sites. For example, dividing  $SA(\delta^{13}C_a)$  by two standard deviations of IAV yields a "signal-to-noise" ratio (Keller et al., 2014) below 2.7 at SH sites and as low as 1.1 at the South Pole and American Samoa (Table 1). Thus,  $SA(\delta^{13}C_a)$  would need to roughly double over the observational period for a trend in  $SA(\delta^{13}C_a)$  to emerge from the noise of IAV at these two sites. The situation is more favourable for trend detection at NH extratropical sites (Table 1), where the signal-to-noise ratio ranges between 9 and 16 and changes of 6 to 11% in  $SA(\delta^{13}C_a)$  would emerge. The Scripps data, including seasonality, are provided as (i) monthly samples, (ii) a fit to these monthly samples, and (iii) the monthly samples but missing values replaced with fitted values. We also used the original, non-gap-filled data and years with at least 9, 10, or 11 monthly values per year in the regression. Trends in  $SA(\delta^{13}C_a)$  from the Scripps gap-filled data are not statistically different from zero, except at the tropical site Christmas Island and the South Pole (Fig. 3). Averaging the trends across all 8 sites yields  $-0.0038 \pm 0.026$  permil/century (mean  $\pm$  1 sdv of mean) and averaging the trends for the extratropical sites ALT, PTB, and LJO yields  $+0.09 \pm 0.06$  permil/century, with both averaged trends not statistically different from zero. Trends are identified for CHR and SPO, whereas the trends at all other sites remain indistinguishable from zero (an exception is MLO when setting the data availability limit to 10 monthly values). The trend for the NH extratropical sites translates into a change in  $SA(\delta^{13}C_a)$  of around  $5 \pm 3\%$  over the 40-year observational period. For the fitted data, trends are statistically different from zero only at two sites (La Jolla and Christmas Island). This is consistent with Gonsamo et al. (2017) who did not detect a temporal trend in  $SA(\delta^{13}C_a)$  and seasonal phasing by fitting Scripps daily flask data from the four sites Alert, Point Barrow, La Jolla, and Mauna Loa. In summary, observed temporal trends in  $SA(\delta^{13}C_a)$  are small ( $\leq 0.15$  permil/century) and not statistically different from zero (at  $p < 0.05$ ) at individual sites. A significant negative trend is found for the tropical site Christmas Island and detection of trends is difficult at the Southern Hemisphere sites, where  $SA(\delta^{13}C_a)$  is small.

The  $\delta^{13}C_a$  records of GLOBALVIEW-CO2C13 (2009) span order of a decade and are, therefore, not used for trend detection, although we evaluated trends from the simulations for the GLOBALVIEW sites (Table 2; excluding Key Biscayne). We require at least 10 monthly values for a year to be included in the linear regression. A limitation of our study is that transport matrices are only available for the period 1982 to 2012, limiting the analysis period and direct model-data comparison to three decades only. Simulated trends in  $SA(\delta^{13}C_a)$  are small (often less than  $0.01\%$  per decade) and statistically insignificant (5% level) except at three SH sites (Ascension, Mahe, South Pole), with a small seasonal cycle amplitude (Table 2). Observed relative trends in  $SA(C_a)$  are larger than in  $SA(\delta^{13}C_a)$  at northern high latitudes and statistically significant at Alert, Point Barrow, Ocean Station, and Mahe Island but insignificant at all other sites over the 1982-2012 analysis period. Simulated trends in  $SA(C_a)$  are insignificant, except at four SH sites and the Mariana Islands.



We compare model ( $m$ ) and observed ( $o$ ) slopes ( $\beta$ ) to probe model-observation agreement. Under the null hypothesis of no slope difference, the  $T = (\beta_m - \beta_o) / \sqrt{s_{\beta_m}^2 + s_{\beta_o}^2}$  statistic (where  $s_{\beta}$  is the standard error of the  $\beta$  slope estimate) is Student t-distributed (Welch, 1947). Trends are different when the  $T$  values are larger than the 0.975 quantile of a t-distribution with  $\nu$  degrees of freedom ( $T > \sim T > \sim 2$ ). ~~Modeled-Modelled~~ and observed trends are different at one site, South Pole, for  $SA(\delta^{13}C_a)$  and at one site (Barrow) for  $SA(C_a)$ . As will become clear in the next section, the largest surface-atmosphere isotope fluxes and temporal changes in these fluxes are simulated in the region north of  $40^{\circ}\text{N}$ . We are therefore interested in quantifying how well the model represents temporal changes in  $SA(C_a)$  in this region and over a 40-year period, representative of the  $\delta^{13}C_a$  observational record. For the five NH high-latitude sites with more than twenty years of data, uncertainties in the temporal change of  $SA(C_a)$  range between 5 and 13% at individual sites over a 40-year period. The average trend in  $SA(C_a)$  for these five NH sites (Alert, Barrow, Ocean Station M, Cold Bay, Shemmya Island) is  $4.8 \pm 1.6$  ppm/century ( $31 \pm 10$  %/century) from observations and  $3.8 \pm 1.8$  ppm/century ( $22 \pm 11$  %/century) from the model. The difference between and the uncertainty in these estimates translates into a relative change in  $SA(C_a)$  of around 4% to 5% over a 40-year period. This suggests that our model chain represents well-accurately represents the observed temporal changes in  $SA(C_a)$  in the NH extratropical atmosphere.

Given the mostly insignificant trends at individual sites over the model analysis period 1982-2012, the question arises whether larger trends are detected when considering longer time scales. Century scale trends, or their absence, can be readily estimated in the simulations by comparing  $SA(C_a)$  and  $SA(\delta^{13}C_a)$  for the modern period (1982-2012) ( $E_{\text{standard}}$ ) and the ~~control run under preindustrial conditions~~ preindustrial control ( $E_{\text{control}}$ ) (Table 1; solid red versus dashed blue line in Fig. S3 and S4). For  $C_a$ , a growth in  $SA$  is clearly visible (12.2 ppm to 17.25 ppm at Alert; 6 ppm to 8.3 ppm at Mauna Loa; 1.7 to 2.1 ppm at the South Pole). Across all 19 sites,  $SA(C_a)$  has grown by  $44\% \pm 35\%$  (mean  $\pm$  standard deviation) from 1700 AD to (1982-2012). The growth in  $SA(C_a)$  ranges between 33% and 42% across the 12 extratropical NH sites (Table 1).

For  $\delta^{13}C_a$ , ~~the control simulation exhibits~~  $E_{\text{control}}$  and  $E_{\text{standard}}$  exhibit an almost identical  $SA$  averaged across all 19 sites ( $2\% \pm 16\%$  lower in  $E_{\text{control}}$  than  $E_{\text{standard}}$ ). ~~Larger deviations are found at individual sites than on average (Fig. S4) with a moderately smaller  $SA(\delta^{13}C_a)$  in  $E_{\text{control}}$  at Alert, almost identical results are found at Mauna Loa and a slightly higher  $SA(\delta^{13}C_a)$  is found at the South Pole in  $E_{\text{control}}$  than  $E_{\text{standard}}$ .~~ The change in  $SA(\delta^{13}C_a)$  from preindustrial ( $E_{\text{control}}$ ) to modern ( $E_{\text{standard}}$ ) range between -6% and 9% across the 12 extratropical NH sites, whereas more diverse results (-28% to + 63%) are simulated at the tropical and SH sites (Fig. S4, Table 1). The ~~modelled industrial period~~ change in  $SA(\delta^{13}C_a)$ ,  $S = E_{\text{standard}} - E_{\text{control}}$ , does not emerge from the noise of variability ( $N = \text{two standard deviations from IAV of } E_{\text{standard}}$ ), except at one tropical (Christmas) and three SH sites (Ascension, Mahe, Palmer). ~~We applied the difference of  $SA(\delta^{13}C_a)$  between  $E_{\text{standard}}$  and  $E_{\text{control}}$  as signal  $S$  and two standard deviations from IAV of  $E_{\text{standard}}$  (or from the observations) as noise  $N$  and requiring: we require~~  $|S|/N > 1$  for the signal  $S$  to emerge (Keller et al., 2014). The fact that trends in  $SA(C_a)$  and the near-zero trends in  $SA(\delta^{13}C_a)$  are better identified by the difference between the modern and preindustrial periods than by regression over the modern period motivates us to focus on the comparison between  $E_{\text{standard}}$  vs  $E_{\text{control}}$  in the remaining result sections.

### 4.3 Zonal decomposition of seasonal land-biosphere fluxes

#### 4.3.1 Changes in the seasonal amplitude of land-biosphere fluxes and $\delta^{13}\text{C}_a$ over the historical period

Next, we address the near-absent temporal trends in  $SA(\delta^{13}\text{C}_a)$  at NH sites by analyzing the zonally-averaged cumulative  
390 growing season flux of  $|\delta^{13}f_{al,net}^*|$ , i.e.,  $SA(\delta^{13}f_{al,net}^*)$  (Fig. 4). The northern mid- to high-latitude ecosystem fluxes exhibit  
the largest seasonal cycle, followed by tropical rain-green forests and savannahs in  $E_{\text{standard}}$ . This flux pattern contributes to  
the larger  $SA(\delta^{13}\text{C}_a)$  at the NH extratropics versus tropical and SH sites. A similar latitudinal flux pattern holds for  $E_{\text{control}}$ .

Turning to the change over the historical period,  $SA(\delta^{13}f_{al,net}^*)$  is 28% larger for the region north of  $15^\circ\text{N}$  (30% larger  
for  $>40^\circ\text{N}$ , and 20% larger for  $15^\circ\text{N}$ - $40^\circ\text{N}$ ) for  $E_{\text{standard}}$  than  $E_{\text{control}}$ . This growth is comparable to the observed increase  
395 in ~~atmospheric  $\text{CO}_2$~~   $C_a$  of 32% from pre-industrial to the reference period of 1982-2012. In contrast,  $E_{\text{control}}$  sometimes  
~~exhibits~~ larger  $SA(\delta^{13}f_{al,net}^*)$  than  $E_{\text{standard}}$  in the tropical and SH ecosystems (Fig. 4). Following Eq. 8, the near-  
proportional growth in the  $SA(\delta^{13}f_{al,net}^*)$  and annual mean ~~atmospheric  $\text{CO}_2$~~   $C_a$  in the NH extratropics is consistent with  
the absence of any major long-term change in  $SA(\delta^{13}\text{C}_a)$  at extratropical NH sites (Table 1 and Fig. S4).  $SA(\delta^{13}\text{C}_a)$  and its  
change at extratropical NH sites is dominated by the large  $SA(\delta^{13}f_{al,net}^*)$  in the northern extratropics (Fig. 4) and transport  
400 from low latitude regions is less important. On the other hand, the large extratropical  $SA(\delta^{13}f_{al,net}^*)$  influences  $SA(\delta^{13}\text{C}_a)$   
and its temporal changes at lower latitudes. Without this influence, we would, based on Eq. 8, expect a decrease in  $SA(\delta^{13}\text{C}_a)$   
outside the extratropics, given the relative increase in annual mean  ~~$\text{CO}_2$~~   $C_a$  is larger than the increase in  $SA(\delta^{13}f_{al,net}^*)$  in  
these regions.

Factorial simulations, with an individual forcing kept at preindustrial, show small individual contributions by climate change,  
405 fossil emissions, and land use to the industrial period growth in  $SA(\delta^{13}\text{C}_a)$  at northern extratropical sites (Fig. S3 and S4).  
This suggests that the statistically insignificant trend in  $SA(\delta^{13}\text{C}_a)$  at northern extratropical sites is not caused by offsetting  
impacts of climate change versus increasing  $C_a$ . Fossil fuel emissions cause an increase and land use change a reduction in  
 $SA(\delta^{13}\text{C}_a)$  at low latitude and southern sites (Fig. S3 and S4). We attribute the dampening influence of land use change to  
the replacement of  $C_4$  plants by  $C_3$  crops causing a general shift in the fractionation during photosynthesis to less negative  
410 values south of  $\sim 45^\circ\text{N}$  (Fig. 4c). This damping influence highlights the importance of considering spatiotemporal variations  
in  $C_3$  and  $C_4$  plant distributions when analyzing  $\delta^{13}\text{C}_a$ . In summary, the results suggest that the near-proportional growth in  
 $SA(\delta^{13}f_{al,net}^*)$  and in  $C_a$  is mainly responsible for the statistically insignificant trend in  $SA(\delta^{13}\text{C}_a)$  at high northern latitude  
sites, and contributing to the statistically insignificant trend in  $SA(\delta^{13}\text{C}_a)$  at other NH sites via atmospheric transport.

For  $\text{CO}_2$ , the amplitude of the ~~modeled~~ ~~modelled~~ zonally-averaged net atmosphere-to-land  $\text{CO}_2$  flux,  $SA(f_{al,net})$ , shows the  
415 largest values in the NH extratropics and a large increase over the historical period of 33% in the region  $15^\circ\text{N}$ - $90^\circ\text{N}$  ( $15^\circ\text{N}$ -  
 $40^\circ\text{N}$ : 26% ;  $40^\circ\text{N}$ - $90^\circ\text{N}$ : 37%), driven by a larger increase in NPP than release fluxes ( $R$ ), whereas  $SA(f_{al,net})$  is smaller in the  
tropics and SH and shows hardly any changes from preindustrial ( $E_{\text{control}}$ ) to modern ( $E_{\text{standard}}$ ) south of  $20^\circ\text{N}$ . These results  
are consistent with previous studies showing northern ecosystems progressively taking up more carbon during the growing  
season (Graven et al., 2013; Forkel et al., 2016; Piao et al., 2018; Bastos et al., 2019). For example, Bastos et al. (2019), using

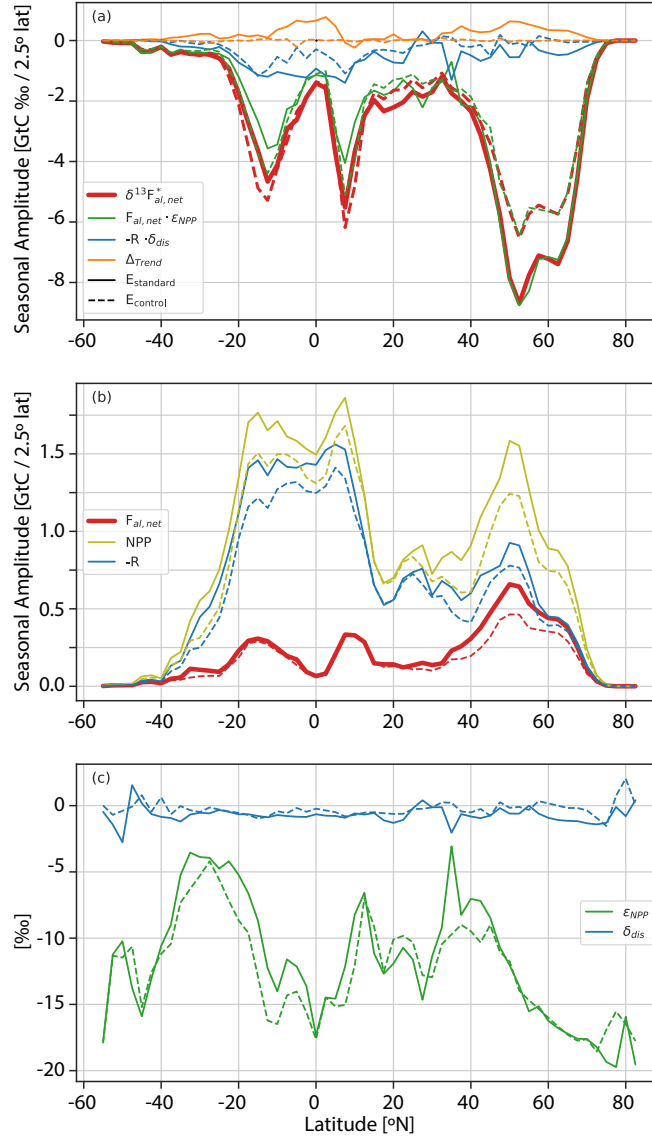


**Figure 4.** The seasonal amplitude per  $2.5^\circ$  latitude band of the signature-weighted, detrended net atmosphere-land flux  $\delta^{13}f_{al,net}^*$  in the period 1982-2012 is shown in panel (a) in red (see Eq. 8). This quantity is the sum of three constituents seasonal amplitudes (Eq. 9 and Appendix A): Net land-atmosphere flux weighted with photosynthetic fractionation ( $f_{al,net} \cdot \epsilon_{NPP}$ , green) plus release fluxes weighted with the disequilibrium signature ( $R \cdot \delta_{dis,la}$ , blue) plus the contribution to the seasonal amplitude by the underlying trend of  $\delta^{13}f_{al,net}^*$  ( $\Delta_{trend}$ , orange) (sign convention: "green+blue+orange=red"). In panel (b), the seasonal amplitudes of (non-detrended) net carbon fluxes are shown. The net atmosphere-land flux ( $f_{al,net}$ , red) is split in Net Primary Productivity (NPP, olive) and release flux ( $R$ , blue). In the bottom panel (c) the corresponding fractionation of photosynthesis  $\epsilon_{NPP}$  and the disequilibrium signature  $\delta_{dis,la}$  is shown. All values are for the period with  $\delta^{13}f_{al,net}^*$  smaller than zero ( $\sim$  growing season). The y-axis in panel (a) is inverted to illustrate the anticorrelation of  $\delta^{13}C$  and carbon fluxes. The results from the standard simulation ( $E_{standard}$ , solid lines) are compared to the preindustrial control simulation ( $E_{control}$ , dashed lines).

420 [carbon fluxes from two atmospheric inversions and 11 land models, find a positive trend in  \$SA\(f\_{al,net}\)\$  north of 40°N and small or no growth in  \$SA\(f\_{al,net}\)\$  between 25°N and 40°N.](#)

### 4.3.2 The coupling between the seasonal amplitude of $C_a$ and $\delta^{13}C_a$

$SA(C_a)$  and  $SA(\delta^{13}C_a)$  are partly coupled by the underlying carbon fluxes. The question arises to which extent  $SA(\delta^{13}C_a)$  holds information independent from  $SA(C_a)$ . We decompose  $\delta^{13}f_{al,net}^*$  in a contribution linked to the net atmosphere-to-land  
425 carbon flux,  $f_{al,net}=NPP-R$ , and an isotopic disequilibrium flux (see Appendix A and section 3 for notation;  $f_{al,net}$  is positive for a flux into the land biosphere):

$$\delta^{13}f_{al,net}^* = \underbrace{(NPP - R)}_{f_{al,net}} \cdot \varepsilon_{NPP} - R \cdot \underbrace{(\delta^{13}C_R - \delta^{13}C_{NPP})}_{\delta_{dis,la}}. \quad (9)$$

NPP is the net primary productivity of all plants within a grid cell.  $R$  is the sum of all land biosphere release fluxes to the atmosphere, such as those from heterotrophic respiration, fire, mortality, and product pools, except autotrophic respiration.  
430  $\delta^{13}C_R$  is the signature of  $R$  and  $\delta^{13}C_{NPP}$  is the signature of NPP, with  $\varepsilon_{NPP}$  (or  $\varepsilon_{al}$ ) representing the (flux-weighted) fractionation by NPP. The difference in signatures of  $R$  and NPP is the isotopic disequilibrium,  $\delta_{dis,la}$ . [Here, as in LPX-Bern, we have assumed that the uptake difference between gross primary production \(GPP\) and NPP is released on short time scales and without further carbon isotope fractionation.](#)

Eq. 9, together with Eqs. 7 and 8, provide insights into the driving factors for the seasonal amplitudes. Putting the ocean  
435 aside (Heimann et al., 1989),  $SA(C_a)$  is driven by the spatio-temporal pattern of  $(NPP-R)$ , whereas  $SA(\delta^{13}C_a)$  is additionally influenced by seasonal variations in  $\varepsilon_{NPP}$ , and the disequilibrium flux  ~~$(R \cdot \delta_{dis,la})$~~  [-  \$R \cdot \delta\_{dis,la}\$](#) . [The latter is indicative of the transit time of carbon through the land biosphere.](#)

The decomposition of zonally-averaged  $SA(\delta^{13}f_{al,net}^*)$  into the amplitude of constituent fluxes and their isotopic signatures is displayed in Figure 4 and Table S1. On the global average,  ~~$SA(f_{al,net} \cdot \varepsilon_{NPP})$ , the amplitude of the net atmosphere-land  
440 flux  $(f_{al,net})$  weighted with the signature of photosynthesis  $(\varepsilon_{NPP})$ ,  $f_{al,net} \cdot \varepsilon_{NPP}$~~  contributes with a fraction of 90% to  $SA(\delta^{13}f_{al,net}^*)$  for both  $E_{standard}$  and  $E_{control}$ . For the region north of 40°N,  ~~$SA(-R \cdot \delta_{dis,la})$ , the amplitude of the disequilibrium flux,~~ contributes only 7% to  $SA(\delta^{13}f_{al,net}^*)$  in  $E_{standard}$  and is almost negligible for  $E_{control}$  (2%). [This In  \$E\_{control}\$ ,  \$SA\(-R \cdot \delta\_{dis,la}\)\$  and  \$\delta\_{dis,la}\$ , albeit smaller than in  \$E\_{standard}\$ , are not negligible due to the lagged response of the respiration signatures to natural changes in  \$\varepsilon\_{NPP}\$ . A small contribution  \$\(\Delta\_{trend}\)\$  to the isotopic flux seasonality in  \$E\_{standard}\$   
445 \[arises from the secular increase in flux \\(Fig. 4; see Appendix A\\). The\]\(#\) small contribution of the disequilibrium flux  \$\(-R \cdot \delta\_{dis,la}\)\$  relative to the net flux  ~~\$\(f\_{al,net} \cdot \varepsilon\_{NPP}\)\$~~  \[-  \\$f\\_{al,net} \cdot \varepsilon\\_{NPP}\\$\]\(#\) ; Eq. 9\) arises as the seasonal amplitude of the carbon release flux  \$R\$  is similar in magnitude to that of the net land carbon uptake  \$f\_{al,net}\$  in the northern extratropics \(blue vs red lines in Fig. 4b\) while the disequilibrium  \$\delta\_{dis,la}\$  is an order of magnitude smaller than  ~~\$\varepsilon\_{NPP} - \varepsilon\_{NPP}\$~~  \[-  \\$\varepsilon\\_{NPP}\\$\]\(#\)  \(Fig. 4c\). Thus in LPX,  \$SA\(\delta^{13}C\_a\)\$  is dominated by the growing season net carbon uptake flux in northern high-latitudes, suggesting that  \$SA\(\delta^{13}C\_a\)\$  holds little information on the  
450 isotopic disequilibrium at high latitude sites. \[Rather, the additional information of  \\$SA\\(\delta^{13}C\\_a\\)\\$  compared to  \\$SA\\(C\\_a\\)\\$  is in the magnitude of  \\$\varepsilon\\_{NPP}\\$  at northern high-latitude sites.\]\(#\) In contrast, the contribution by the disequilibrium flux  \$SA\(-R \cdot \delta\_{dis,la}\)\$  and](#)

by the net carbon flux  $SA(f_{at,net} - \epsilon_{NPP} f_{gl,net} \cdot \epsilon_{NPP})$  are near-equal in the tropics (10°S-10°N) and the SH (Fig. 4, Table S1). Note that in  $E_{control}$ ,  $SA$  of the disequilibrium flux and the disequilibrium between photosynthesis and respiration (Eq. 9 and Fig. 4), albeit smaller than in  $E_{standard}$ , are not negligible due to the lagged response of the respiration signatures to natural changes in  $\epsilon_{NPP}$ . A small contribution ( $\Delta_{trend}$ ) to the isotopic flux seasonality in  $E_{standard}$  arises from the secular increase in flux (Fig. 4; see Appendix A).  $SA(NPP)$  and suggesting that  $SA(\delta^{13}C_a)$  holds potentially additional information on  $R$  increase from preindustrial to modern not only in northern ecosystems but also in the tropics (Fig. 4b) and carbon turnover in these regions in comparison to  $SA(NPP-R)$  increases in the NH extratropics but does hardly change south of 20°N.  $C_a$ .

The zonal variation in (growing season) photosynthetic fractionation  $\epsilon_{NPP} - \epsilon_{NPP}$  is mainly due to differences in vegetation composition, with  $C_4$  plants having considerably lower photosynthetic fractionation than  $C_3$  plants (Fig. 4c). Land use and the evolving distribution of  $C_3$  and  $C_4$  crops are prescribed in the model and  $C_4$  grasses are more prevalent than  $C_3$  grasses in low-latitude dryland ecosystems. Accordingly, maxima in flux-weighted, zonal-mean  $\epsilon_{NPP} - \epsilon_{NPP}$  are simulated at 35°N, 12°N, and broadly around 30°S. Minima are simulated for the  $C_3$ -dominated  $C_3$ -dominated high-latitude ecosystems and tropical rain forest zone. In  $E_{standard}$   $\epsilon_{NPP} - \epsilon_{NPP}$  is generally less negative than in  $E_{control}$  and increased by 1.18 ‰ (9% in relative units) on the global average ( $SA(NPP)$ -weighted) mainly due to the increase in the prevalence of  $C_4$  plants  $C_4$  plants, while  $\epsilon_{NPP}$  remains time-invariant in the  $C_3$ -dominated ecosystems north of 45°N (Fig. 4c). To estimate the influence of the increase in  $C_4$  prevalence on global mean  $\epsilon_{NPP} - \epsilon_{NPP}$  (but not on global GPP), we run a factorial simulation,  $E_{C_3}$ , with the fractionation formulation for all  $C_4$  plants replaced by those for  $C_3$  plants. The difference between  $E_{standard}$  and  $E_{C_3}$ , i.e., the change in fractionation attributable to  $C_4$  plants, amounts to about 1.5 ‰ on global average (1982-2012 versus 1720-1750) (Fig. S5). The disequilibrium signature  $\delta_{dis,ta}$  is closer to zero for the control than the standard simulation. This is expected because the signal from the atmospheric  $^{13}C$ , pointing again to the importance of  $C_3/C_4$  Suess effect in  $R$  is delayed relative to NPP by vegetation, soil, and product pool lifetimes, leading to a disequilibrium with respect to the production signature.

## 5 Discussion

### 4.1 Growth in seasonal cycle amplitudes: implications for stomatal conductance and water use

#### 4.1.1 plant distribution changes for $\delta^{13}C_a$

The seasonal amplitude of  $CO_2$  ( $SA(C_a)$ ) is observed to grow over time depending on location (Bacastow et al., 1985; Barlow et al., 2015) and driven by Keeling et al. (2017) analyzed the atmospheric budgets of carbon and  $^{13}C$ , using seasonally detrended data, a three-box land model with time-invariant overturning timescales, globally uniform isotopic fractionation, and neglecting changes in  $C_3/C_4$  distribution in their standard setup. They found global mean  $\epsilon_{NPP}$  to decrease by  $0.66 \pm 0.34$  ‰ from 1975 to 2005 and attributed this change to changes in fractionation associated with mesophyll conductance and photorespiration of  $C_3$  plants. It appears challenging to detect and attribute changes in the seasonality of net land carbon uptake (Graven et al., 2013; Forkel et al., 2016). The growth is captured by our model and simulated and observations-based trends generally agree within uncertainties at individual stations. Averaging the signals across northern high-latitude sites ( $>40^\circ N$ ), yields relatively small uncertainties in

485 data and model slopes and their difference, corresponding to a change in seasonal amplitude of 5% ( $1-\sigma$ ) over a 40-year period. Corresponding uncertainties and data-model mismatches in slopes are up to 21% for the individual high latitude sites. The good data-model agreement for the averaged trend suggests that our model chain broadly captures fractionation of global mean NPP with a box model, given uncertainties in NPP (Graven et al., 2024) and changes in  $C_3$  versus  $C_4$  plant distribution.

490 While the influence of trends in the seasonal cycle of net land carbon uptake on trends in  $SA$  (the gross exchange flux and the isotopic disequilibrium on  $\delta^{13}C_a$ ) and  $SA(\delta^{13}C_a)$  seasonality is modelled to be small at northern sites –

Previous studies show northern ecosystems progressively taking up more carbon during the growing season (Graven et al., 2013; Forkel et al., 2019). For example, Bastos et al. (2019) find a positive trend in  $SA(f_{al,net})$  north of  $40^\circ\text{N}$  and small or no growth in  $SA(f_{al,net})$  between  $25^\circ\text{N}$  and  $40^\circ\text{N}$ . Consistent with these studies, the seasonal cycle amplitude of NPP and the terrestrial release flux  $R$  is simulated by LPX-Bern to increase over the industrial period in both hemispheres, but the growing season net carbon uptake ( $SA(\text{NPP}-R)=SA(f_{al,net})$ ) is only increasing north of  $\sim 30^\circ\text{N}$  (Fig. 4b).

495 For  $\delta^{13}C_a$ , the observations from the (GLOBALVIEW-CO2C13, 2009) and Scripps products do not show a statistically significant change of  $SA(\delta^{13}C_a)$  at most sites with more than 20 years of data (Fig. 3). This is consistent with Gonsamo et al. (2017) who did not detect a temporal trend in  $SA(\delta^{13}C_a)$  and seasonal phasing by fitting Scripps daily flask data from the four sites Alert, Point Barrow, La Jolla, and Mauna Loa. Modeled changes in  $SA(\delta^{13}C_a)$  yield no clear trend in the standard case over the simulation period 1982 to 2012, consistent with the observations. Further,  $SA(\delta^{13}C_a)$  is in general very similar for the preindustrial control and the standard case at the NH sites (Table 1; dashed blue vs red line in Supplementary Fig. S4), again consistent with the statistically insignificant trend in the observations.

Theoretical considerations imply no trend in  $SA(\delta^{13}C_a)$  for a proportional growth in the seasonality of net atmosphere-surface isotope flux ( $\sim SA(\delta^{13}f_{al,net}^*)$ ) and in background atmospheric  $\text{CO}_2$  (see Eq. 8 section 3). Both parameters increased by about 30% over the industrial period over northern ecosystems ( $>40^\circ\text{N}$ ). The growth in  $SA(\delta^{13}f_{al,net}^*)$  is primarily driven by the increase in growing season net carbon uptake ( $SA(f_{al,net})$ ) at northern latitudes. We suggest that the near-proportional growth in  $SA(\delta^{13}f_{al,net}^*)$  and in background atmospheric  $\text{CO}_2$  is mainly responsible for the statistically insignificant trend in  $SA(\delta^{13}C_a)$  at high northern latitude sites, and contributing to the statistically insignificant trend in  $SA(\delta^{13}C_a)$  at other NH sites via atmospheric transport. Factorial simulations, with an individual forcing kept at preindustrial, show small individual contributions by climate change, fossil emissions, and land use to the industrial period growth in  $SA$  (for today, it remains to be explored how global warming will change these parameters, e.g., due to changes in fire frequency and tree mortality, and affect  $\delta^{13}C_a$  and the information provided by continued  $\delta^{13}C_a$ ) at northern extratropical sites (Fig. S3 and S4). This suggests that the statistically insignificant trend in  $SA$  (observations. We may also expect different disequilibrium fluxes and, in turn,  $\delta^{13}C_a$ ) at northern extratropical sites is not caused by offsetting impacts of climate change versus increasing  $\text{CO}_2$  seasonality if the global carbon sink is driven by a stimulation of NPP, e.g., by  $\text{CO}_2$ . Fossil fuel emissions cause an increase and land use change a reduction in fertilization (Walker et al., 2021) as in LPX-Bern, versus a change in tree longevity (Bugmann and Christof, 2011; Körner, 2017). It remains to investigate, e.g., by applying perturbed parameter ensembles and sensitivity simulations, whether such differences indeed significantly affect  $\delta^{13}C_a$  seasonality.

Monitoring  $C_a$  and  $\delta^{13}C_a$  over tropical and SH land regions could potentially provide valid information to disentangle NPP, respiration, and net carbon fluxes given the substantial contribution of the disequilibrium flux to  $SA(\delta^{13}C_a^{f*})$ . However, the seasonality of  $\delta^{13}C_a$  at low latitude and southern sites (Fig. S3 and S4). We attribute the dampening influence of land use change to the replacement of C4 plants by C3 crops causing a general shift in the fractionation during photosynthesis to less negative values south of  $\sim 45^\circ\text{N}$  (Fig. 4c). This damping influence highlights the importance of considering spatiotemporal variations in C3 and C4 plant distributions when analyzing  $\delta^{13}C_a$  and  $C_a$  at the tropical background monitoring sites analyzed in this study is strongly influenced by long-range transport, adding uncertainty to the interpretation of seasonal signals at background sites. Ideally, seasonally-resolved observations are taken in air masses influenced primarily by regional land biosphere fluxes, thereby minimizing uncertainties from long-range transport, and interpreted with the help of atmospheric transport and land biosphere models (Botía et al., 2022). For example, the data may be assimilated into atmospheric transport models applied in inverse mode to infer surface carbon and isotope fluxes or into isotope-enabled land biosphere models, combined with atmospheric transport, to optimize parameters governing modelled carbon and isotope fluxes (Peylin et al., 2016; van der Ve

#### 4.4 Implications for stomatal conductance and water use

Our results result of a time-invariant  $\varepsilon_{\text{NPP}}$  in northern extratropical regions hold implications for carbon and water fluxes, and evaporative cooling. The good agreement between observations and model results for  $SA(\delta^{13}C_a)$  and its temporal trend at northern sites provides implicit support for regulation of stomatal conductance by C3-C3 plants towards a constant ratio of the  $\text{CO}_2$  mole fraction in the leaf intercellular space ( $c_i$ ) and ambient atmospheric air ( $c_a$ ) on the continental scale. Following Farquhar (1989), the fractionation for C3 photosynthesis and NPP (and Cernusak et al. (2013),  $\varepsilon_{\text{NPP}}$ ) is approximately proportional to  $c_i/c_a$ :  $\varepsilon_{\text{NPP}} = a + (b - a) \cdot \frac{c_i}{c_a}$ ,

$$\varepsilon_{\text{NPP}} = - \left( a + (b - a) \cdot \frac{c_i}{c_a} \right), \quad (10)$$

with  $a$  (4.4), and  $b$  (27) being constants. Two contrasting scenarios are published for the regulation of leaf stomatal conductance for C3-C3 plants. First, many site studies (Voelker et al., 2016; Saurer et al., 2014; Kauwe et al., 2013; Peñuelas et al., 2011; Frank et al., 2015; Keller et al, 2017) suggest a regulation of stomatal conductance towards a constant  $c_i/c_a$  and, hence,  $c_i$  to grow proportional to  $c_a$ . An absent temporal trend in  $c_i/c_a$  translates into an absent trend in  $\varepsilon_{\text{NPP}}$ , and vice versa (Eq. 10). Focusing on regions north of  $>40^\circ\text{N}$ , where carbon fluxes are largest and C3-C3 plants dominate, LPX-Bern simulates a small role of isotopic disequilibrium fluxes and a dominant influence of net atmosphere-surface fluxes on  $SA(\delta^{13}C_a)$  (Fig. 4, green vs blue lines). Importantly, LPX-Bern simulates small temporal changes in the (flux-weighted) fractionation of the zonally and seasonally integrated NPP at northern sites (Fig. 4c, green lines) and a stomatal regulation towards constant  $c_i/c_a$ . In turn, the good model-data agreement in the temporal trends of  $SA(C_a)$  and  $SA(\delta^{13}C_a)$  imply consistency with the observational evidence for this scenario towards constant  $c_i/c_a$ .

550 In contrast, [Battipaglia et al. \(2013\)](#) and [Keenan et al. \(2013\)](#) [Battipaglia et al. \(2013\)](#) and [Keenan et al. \(2013\)](#) suggest a regulation of stomatal conductance towards a constant  $c_i$  and a decreasing ratio  $c_i/c_a$  under rising  $\text{CO}_2$ . Evaluating Eqs. 10 for 1980-2022, the period with  $\delta^{13}\text{C}_a$  measurements, yields a decrease in  $\varepsilon_{\text{NPP}}$  of 15% (-3.0 to -3.8 ‰) for an initial  $c_i/c_a$  ratio in the range of 0.7 to 0.9 and constant  $c_i$ . We argue that the good observation-model agreement in the simulated trends in  $SA(C_a)$  implies that the influence of the simulated net atmosphere-land carbon flux is realistic and  $SA(\delta^{13}\text{C}_a)$  would decrease if  $\varepsilon_{\text{NPP}}$  decreases. A decrease in  $SA(\delta^{13}\text{C}_a)$  of 15% would emerge from the noise of variability at individual northern sites. Taken together, we suggest that the scenario towards constant  $c_i/c_a$  is consistent with the observations whereas the scenario towards constant  $c_i$  appears less likely. However, uncertainties remain and our conclusions for the two scenarios of stomatal regulation await confirmation by other modelling studies.

The two scenarios imply large differences in water fluxes (Knauer et al., 2017). The intrinsic water use efficiency (iWUE), the ratio between assimilation of  $\text{CO}_2$  by photosynthesis ( $A$ ) and conductance of  $\text{CO}_2$  ( $g$ ), is, as  $\varepsilon_{\text{NPP}}$ , a function of  $c_i$  and  $c_a$ :

$$iWUE = \frac{A}{g} = c_a \cdot \left(1 - \frac{c_i}{c_a}\right). \quad (11)$$

iWUE would have increased from 1980 to 2022 by 23% for  $c_i/c_a$  constant, but by 77 to 231% for  $c_i$  constant, assuming an initial  $c_i/c_a$  of 0.7 to 0.9. In the latter scenario, stomatal conductance and, correspondingly, water loss per stomatal pore, would have decreased strongly over the last decades.

Equation 10 is an approximation (Farquhar et al., 1982; Lloyd and Farquhar, 1994; Farquhar and Cernusak, 2012; Cernusak et al., 2013) considered to be sufficient for many applications by Cernusak et al. (2013) and applied in the publications cited in the previous two paragraphs. However, there are four contributions only implicitly considered by choosing parameter  $b$  in Eq. 10 and these may contribute small temporal trends to  $\varepsilon_{\text{NPP}}$ . In turn, inferred  $c_i/c_a$  would also have a temporal trend for a constant  $\varepsilon_{\text{NPP}}$ . We estimate the trend contribution of these additional terms to be of small magnitude (<1 ‰) in comparison to the 3 to 3.8 ‰ difference estimated for our two scenarios (see Appendix B for details).

#### 4.2 Seasonality: $C_a$ versus $\delta^{13}\text{C}_a$ and isotopic disequilibrium

Observations of  $\delta^{13}\text{C}_a$  seasonality provide different, complementary information compared to observations of  $C_a$  seasonality. As discussed above, the model results suggest that the additional information of  $SA(\delta^{13}\text{C}_a)$  compared to  $SA(C_a)$  is in the magnitude of  $\varepsilon_{\text{NPP}}$  at northern high-latitude sites. The contribution of the isotopic disequilibrium flux, indicative of the transit time of carbon through the land biosphere, plays a relatively small role in the northern extratropics, given the large growing season net carbon uptake flux in this region (Fig. 4). In contrast, for tropical and SH ecosystems, the terrestrial isotopic disequilibrium flux plays a large role (blue versus green line in Fig. 4a), at least in our model. However, the seasonality of  $\delta^{13}\text{C}_a$  and  $C_a$  at the tropical background monitoring sites analyzed in this study is strongly influenced by long-range transport, adding uncertainty to the interpretation of seasonal signals. Further, we have limited understanding of net ecosystem exchange in the tropics, and uptake and release fluxes may cancel largely in the evergreen rain forest limiting the value of



seasonal analyses in this biome. Monitoring  $C_a$  and  $\delta^{13}C_a$  over tropical and SH land regions could potentially provide valid information to disentangle NPP, respiration, and net carbon fluxes. Ideally, seasonally-resolved observations are taken in air masses influenced primarily by regional land biosphere fluxes, thereby minimizing uncertainties from long-range transport, and interpreted with the help of atmospheric transport and land biosphere models (Botía et al., 2022). For example, the data may be assimilated into atmospheric transport models applied in inverse mode to infer surface carbon and isotope fluxes or into isotope-enabled land biosphere models, combined with atmospheric transport, to optimize parameters governing modelled carbon and isotope fluxes (Peylin et al., 2016; Castro-Morales et al., 2019).

While the influence of the gross exchange flux and the isotopic disequilibrium on  $\delta^{13}C_a$  seasonality is modeled to be small at northern sites for today, it remains to be explored how global warming will change these parameters, e.g., due to changes in fire frequency and tree mortality, and affect  $\delta^{13}C_a$  and the information provided by continued  $\delta^{13}C_a$  observations. We may also expect different disequilibrium fluxes and, in turn,  $\delta^{13}C_a$  seasonality if the global carbon sink is driven by a stimulation of NPP, e.g., by  $CO_2$  fertilization (Walker et al., 2021) as in LPX-Bern, versus a change in tree longevity (Bugmann and Christof, 2011; Körner, 2011). It remains to investigate, e.g., by applying perturbed parameter ensembles and sensitivity simulations, whether such differences indeed significantly affect  $\delta^{13}C_a$  seasonality.

The role of isotopic disequilibrium fluxes depends on the timescales considered. Analyses of the global budget of annual-mean atmospheric  $\delta^{13}C(CO_2)$  (Keeling et al., 1989; Francey et al., 1995; Joos and Bruno, 1998; Trudinger et al., 2002; van der Velde et al., 2011) indicate that the emissions of isotopically-light carbon from fossil fuel burning are primarily balanced by a reduction in the atmospheric inventory and ocean and land disequilibrium fluxes, leaving a relatively small role for the isotopic flux associated with the net ocean and land carbon sink. Ocean and land fluxes are about equally important for the removal of the fossil fuel  $\delta^{13}C(C_a)$  perturbation. For the seasonality of  $\delta^{13}C(C_a)$ , our results confirm that the land fluxes exert a dominant influence compared to ocean fluxes at NH sites and we find, on the global average, that the disequilibrium flux contributes a small fraction to the seasonal amplitude of the net land isotope flux.

On a technical note, transporting simulated  $^{13}C$  fluxes is not without challenges. The definition of the  $\delta$ -notation can pose numerical difficulties when net  $^{12}C$  fluxes are close to zero. We find that transporting signature-weighted total carbon fluxes is the most reliable method for arriving at local  $\delta^{13}C_a$ . Similarly, seemingly small errors in the model representation of gross fluxes and mass balances, can become critical when considering net surface-to-atmosphere fluxes.

## 5 Conclusions

In conclusion, we explored the global-scale mechanisms driving the observed seasonal cycle of atmospheric cycles of  $\delta^{13}C$  (of atmospheric  $CO_2$ ) and ( $\delta^{13}C_a$ ) and of atmospheric  $CO_2$  at 19 monitoring sites using atmosphere-surface fluxes from the Bern3D-LPX Earth System Model of Intermediate Complexity and fossil emissions in combination with transport matrices from the TM3 atmospheric transport model. We find good data-model agreement at northern and tropical sites. No significant trends are detected nor modeled-modelled in the seasonal cycle amplitude of  $\delta^{13}C(CO_2)_a$  at most monitoring sites, in contrast to the positive trends in the seasonal amplitude of  $CO_2$ . We attribute the statistically insignificant trend in the

615 seasonal amplitude of  $\delta^{13}\text{C}(\text{CO}_2)\text{-}C_a$  to a near-equal percentage increase in the growing season net carbon uptake and isotope flux and the background atmospheric  $\text{CO}_2$  in the northern extratropical land regions. Over the industrial period and at low-latitude and SH sites, land use change has a dampening influence on  $\delta^{13}\text{C}_a$  seasonality through the replacement of ~~C3-plants~~ ~~by C4-C3 plants~~ ~~by C4~~ crops. ~~Modeled~~ Modelled isotopic disequilibrium fluxes have a small influence on the seasonal signal of  $\delta^{13}\text{C}(\text{CO}_2)\text{-}C_a$  at NH sites, but play an important role in ~~tropic-tropical~~ and SH ecosystems, suggesting that monitoring the  $\delta^{13}\text{C}_a$  seasonality over tropical and SH land would provide valuable information on gross carbon exchange fluxes and the time scales of carbon turnover in the land biosphere. Our results, based on a single model chain, provide implicit support for a regulation of the stomatal conductance of ~~C3-C3~~ plants towards a constant  $c_i/c_a$  on biome scales and intrinsic water use efficiency to grow proportionally to atmospheric  $\text{CO}_2$  over recent decades with implications for carbon and water fluxes. More generally, the results suggest that observations of the  $\delta^{13}\text{C}_a$  seasonal cycle offer highly useful information on carbon and water cycle processes. We recommend ~~to apply~~ applying seasonally-resolved  $\delta^{13}\text{C}_a$  observations as a ~~novel~~ constraint for land biosphere models used to simulate the terrestrial sink of anthropogenic carbon and land use emissions, for example, by using perturbed parameter ensembles in Bayesian approaches (Lienert and Joos, 2018; van der Velde et al., 2018). Future studies may employ an ensemble of ~~isotope-enabled~~ isotope-enabled models and perturbed parameter ensembles to elucidate whether our findings are robust and which models or process assumptions are compatible or incompatible with  $\delta^{13}\text{C}_a$  data for improved projections of atmospheric  $\text{CO}_2$  and global warming.

*Code and data availability.* The data from the Scripps  $\text{CO}_2$  program are available here: [https://scrippsco2.ucsd.edu/data/atmospheric\\_co2/](https://scrippsco2.ucsd.edu/data/atmospheric_co2/) (last access: 17.04.2023). The GLOBALVIEW data from the Global Monitoring Laboratory were downloaded here: <https://gml.noaa.gov/ccgg/globalview/> (last access: 27.04.2022). The data displayed in the Figures will be made freely available at Zenodo or a similar site when the manuscript is accepted. For the review process the data and plotting scripts are available as a download:

635 <https://cloud.climate.unibe.ch/s/g9qrit7KDRnrbLp>

## Appendix A: Decomposition of $\delta^{13}f_{as,net}^*$ and the calculation of seasonal amplitudes

We reformulate the net isotope flux in terms of net and gross carbon fluxes, isotopic fractionation, and isotopic disequilibrium (e.g., Mook 1986; Joos and Bruno 1998) to diagnose their influence on the seasonal cycles.

The fractionation for a gross flux, e.g., from the atmosphere to the surface, is:

$$640 \quad \varepsilon_{as} \cong (\delta^{13}\text{C}_{as} - \delta^{13}\text{C}_a), \quad (\text{A1})$$

with  $\delta^{13}\text{C}_{as}$  the signature of the gross flux from  $a$  to  $s$  ( $f_{as}$ ) and  $\delta^{13}\text{C}_a$  the signature of the source. The isotopic disequilibrium (or difference) between atmosphere-surface gross fluxes is:

$$\delta_{dis,sa} = -\delta_{dis,as} = (\delta^{13}\text{C}_{sa} - \delta^{13}\text{C}_{as}) \quad (\text{A2})$$

The net carbon and isotope fluxes are differences between gross fluxes:

$$645 \quad f_{as,net} = f_{as} - f_{sa} \quad (A3)$$

$$\delta^{13} f_{as,net}^* = f_{as} \cdot (\delta^{13} C_{as} - \delta^{13} C_a) - f_{sa} \cdot (\delta^{13} C_{sa} - \delta^{13} C_a) \quad (A4)$$

Rearranging yields:

$$\delta^{13} f_{as,net}^* = f_{as,net} \cdot \underbrace{(\delta^{13} C_{as} - \delta^{13} C_a)}_{\varepsilon_{as}} - f_{sa} \cdot \underbrace{(\delta^{13} C_{sa} - \delta^{13} C_{as})}_{\delta_{dis,sa}} \quad (A5)$$

650 For the land biosphere (index  $l$ ), it follows from Eqs. A3 and A5:

$$f_{al,net} = \text{NPP} - R \quad (A6)$$

$$\delta^{13} f_{al,net}^* = f_{al,net} \cdot \varepsilon_{\text{NPP}} - R \cdot \delta_{dis,la}, \quad (A7)$$

with:

$$655 \quad \delta_{dis,la} = \delta^{13} C_R - \delta^{13} C_{\text{NPP}} \quad (A8)$$

NPP is the net primary productivity of all plants within a grid cell.  $R$  is the sum of all release fluxes to the atmosphere, such as those from heterotrophic respiration, fire, mortality, and product pools, except autotrophic respiration.  $\delta^{13} C_R$  is the signature of  $R$  and  $\delta^{13} C_{\text{NPP}}$  is the signature of NPP, with  $\varepsilon_{\text{NPP}}$  (or  $\varepsilon_{al}$ ) representing the (flux-weighted) fractionation by NPP. **Here, as in LPX-Bern, we have assumed that the uptake difference between gross primary production (GPP) and NPP is released on short time scales and without further carbon isotope fractionation.**

660 The seasonal amplitudes of  $\delta^{13} f_{al,net}^*$  and its components are calculated as follows. The time series of  $\delta^{13} f_{al,net}^*$  is detrended and normalized to zero. The trend is computed by a rolling 12-month mean of  $\delta^{13} f_{al,net}^*$ . Then, the resulting trend curve is subtracted from  $\delta^{13} f_{al,net}^*$  (disregarding the first and last 6 months of the original series) to get a detrended curve. Finally, the detrended curve is normalized by subtracting its period mean.  $\Delta_{trend}$  (e.g., in units of mol permil yr<sup>-1</sup> m<sup>-2</sup>) is the difference between  $\delta^{13} f_{al,net}^*$  after and before this detrending and normalizing procedure. We define a seasonal mask to compute seasonal amplitudes of fluxes and their signatures. For each model year, we identify months in which detrended  $\delta^{13} f_{al,net}^*$  is negative or equal to zero (roughly corresponding to the growing season). The sum of fluxes of these months is then termed the "seasonal amplitude" in a given year. For  $\delta^{13} f_{al,net}^*$ , this procedure is consistent with considering the difference between maximum and minimum values of the detrended cumulative sum of  $\delta^{13} f_{al,net}^*$ . Accordingly, the seasonal amplitudes of the component fluxes contributing to  $\delta^{13} f_{al,net}^*$  are computed by summation over months where  $\delta^{13} f_{al,net}^*$  is less or equal to zero within a given year. Component fluxes are  $[(\text{NPP}-R) \cdot \varepsilon_{\text{NPP}}]$ ,  $[R \cdot \delta_{dis,la}]$ ,  $[\Delta_{trend}]$ , and, further,  $[\text{NPP}]$ ,  $[R]$ , and  $[\text{NPP}-R]$  (Fig. 4). These

component fluxes are not detrended to readily calculate the signatures  $\delta_{dis,la}$  and  $\epsilon_{NPP} - \epsilon_{NPP}$  by division of the seasonal amplitude isotopic flux with the corresponding seasonal amplitude carbon flux.

We note that the annual climatological mean values of the isotopic disequilibrium ( $\delta_{dis,la}$ ), the net carbon flux ( $f_{al,net}$ ), and the net isotopic flux ( $\delta^{13}f_{al,net}^*$ ) vanish by definition for the preindustrial equilibrium. However, this does not hold for their seasonal amplitudes. Further, detrending  $\delta^{13}f_{al,net}^*$  before the computation of its seasonal amplitude is consistent with the calculation of the  $C_a$  and  $\delta^{13}C_a$  seasonal amplitude from the detrended atmospheric time series.

The seasonal cycles of  $C_a$  or  $\delta^{13}C_a$  are computed from observations and the TM3 results using the following procedure for either  $C_a$  or  $\delta^{13}C_a$ , respectively. Months with missing values in either the observation or the TM3 simulation are masked in the TM3 and observational time series. Then the time series are detrended using a 12-month rolling mean and the overall mean of the series is set to zero to get for year,  $y$ , and month,  $m$ , seasonal anomalies  $\Delta C_a(y, m)$  and  $\Delta \delta^{13}C_a(y, m)$ . Finally, the period means for each calendar month,  $\overline{\Delta C_a(m)}$  and  $\overline{\Delta \delta^{13}C_a(m)}$ , are computed by averaging over all corresponding monthly values. Additionally, the standard deviation is computed for each calendar month to inform about the interannual variability of the seasonality. The period-mean  $SA$  is computed as the difference between the month with the highest ( $\overline{m_{max}}$ ) and lowest ( $\overline{m_{min}}$ ) value in  $\overline{\Delta C_a(m)}$  and  $\overline{\Delta \delta^{13}C_a(m)}$ , respectively. For individual years, we computed  $SA$  by difference from the extreme monthly values of each year.

## Appendix B: Uncertainties in the relationship between $\epsilon_{NPP}$ and $c_i/c_a$

In section 4.1, we applied a simplified expression for fractionation of  $C_3$  plants during photosynthesis ( $\epsilon_{NPP}$ ) and used this expression to translate trends in  $\epsilon_{NPP}$  to trends in  $c_i/c_a$  and in iWUE. The potential contributions to trends in  $\epsilon_{NPP}$  from neglected ternary effects, “dark” day respiration, and transport through the mesophyll and photorespiration are discussed in this appendix.

Isotopic fraction for  $C_3$  photosynthesis is framed as a multi-step process considering the transport of  $CO_2$  and the underlying gradients in  $CO_2$  mole fractions, from the ambient air (mole fraction:  $c_a$ ) to the leaf surface ( $c_s$ ) in the intercellular air spaces ( $c_i$ ) and the sites of carboxylation ( $c_c$ ) plus the fractionation during carboxylation, “dark” day respiration,  $R_d$ , and photorespiration (Cernusak 2013). The transport of  $CO_2$  equals the consumption of  $CO_2$  by assimilation,  $A$ :  $A = g(c_a - c_i) = g_m(c_i - c_c)$ , with  $g$  being the conductance of the stomatal pores and the boundary layer and  $g_m$  the mesophyll conductance. The relationship can be rewritten as  $A/(g c_a) = (1 - c_i/c_a) = g_m/g(c_i/c_a - c_c/c_a)$ . If  $A$  is increasing in proportion to  $c_a$  and  $g$  and  $g_m$  assumed constant, then it follows that also  $c_i/c_a$  and  $c_c/c_a$  are constant. In turn, the fractionation associated with boundary layer and stomatal conductance ( $-a(1 - c_i/c_a)$ ;  $a = 4.4\%$ ), mesophyll conductance ( $-a_m(c_i/c_a - c_c/c_a)$ ;  $a_m = 1.8\%$ ), and carboxylation ( $-b \times c_c$ ) remain constant. The overall influence of mesophyll transport on  $\epsilon_{NPP}$  can also be written as  $(b - a_m)/g_m \times A/c_a$  (Keeling et al., 2017).

Keeling et al. (2017) assumed that  $A/c_a$  decreases over time, with  $A$  increasing by 45% for a doubling of  $CO_2$ , and that therefore fractionation by the mesophyll contribution would change by  $-0.006\%$  ppm<sup>-1</sup>, i.e., a change in  $\epsilon_{NPP}$  of 0.47‰ for the  $CO_2$  increase of 78 ppm from 1980 to 2022. On the other hand, Campbell et al. (2017) observationally constrained the

705 [growth in gross primary production over the 20th century to be  \$31 \pm 5\%\$ , larger than the increase in  \$c\_a\$  of 25%. Accordingly,  \$A/c\_a\$  increases and the mesophyll trend contribution is positive. With the central parameters values of Keeling et al \( \$A=9 \mu\text{mol m}^{-2} \text{s}^{-1}\$ ,  \$g\_m=0.2 \text{ mol m}^{-2} \text{s}^{-1}\$ ,  \$\text{CO}\_2=355 \text{ ppm}\$ \) the contribution is  \$+0.002\text{‰ ppm}^{-1}\$ . Keeling et al. also estimated changes in fractionation associated with photorespiration \( \$-f \times \Gamma^\*/c\_a\$ ;  \$f = 12\text{‰}\$ \) to  \$-0.004\text{‰ ppm}^{-1}\$  assuming a constant  \$\text{CO}\_2\$  compensation point,  \$\Gamma^\*\$ . The real sensitivity must be smaller as  \$\Gamma^\*\$  increases with temperature and because Keeling et al.](#)  
710 [al. applied an estimate for the  \$\text{CO}\_2\$  compensation point in the presence of  \$R\_d\$  \(43 ppm\) instead of the absence of  \$R\_d\$  \( \$\Gamma^\*=31 \text{ ppm}\$ \). Further, fractionation during day respiration is  \$-e \times c\_c/c\_a \times R\_d/V\_c\$  \(Cernusak et al., 2013\), roughly about 0 to  \$-0.3\text{‰}\$  for  \$e\$  in the range of 0 to  \$5\text{‰}\$ ; we apply a Rubisco carboxylation rates,  \$V\_c\$ , of  \$11 \mu\text{mol m}^{-2} \text{s}^{-1}\$  derived from the value of  \$A=9 \mu\text{mol m}^{-2} \text{s}^{-1}\$  by Keeling et al.,  \$R\_d=1 \mu\text{mol m}^{-2} \text{s}^{-1}\$ , and  \$c\_c/c\_a = 0.6\$ \). Finally, ternary effects of about  \$-0.7\text{‰}\$  \( \$0.024 \times b\$ \) increase with water vapor deficit \(Farquhar and Cernusak, 2012\). Given the small amplitudes of these two contributions, their](#)  
715 [temporal trends are also small over recent decades.](#)

*Author contributions.* FJ and SL wrote the manuscript with inputs from SZ. SL performed all model runs and FJ the statistical analyses. SL and FJ produced the figures and tables.

*Competing interests.* The authors declare to have no competing interests

*Acknowledgements.* This project has received funding from the European Union's Horizon 2020 research and innovation programme under  
720 grant agreement No 821003 (project 4C, Climate-Carbon Interactions in the Current Century) and by the Swiss National Science Foundation (project #200020\_200511). The work reflects only the authors' view; the European Commission and their executive agency are not responsible for any use that may be made of the information the work contains. We thank the researchers of the Cooperative Atmospheric Data Integration Project, NOAA ESRL, Boulder, Colorado, and of the Scripps  $\text{CO}_2$  program for making their  $\text{CO}_2$  and  $\delta^{13}\text{C}$  data freely available and Martin Heimann for suggesting to plot seasonal anomalies of  $\text{CO}_2$  versus those of  $\delta^{13}\text{C}$ . A special thanks goes to Christoph Köstler for  
725 providing the TM3 transport matrices and to Aurich Jeltsch-Thömmes for help with Bern3D. [We thank Gerbrand Koren and an unknown reviewer for their careful reviews and Ji-Hyung Park for editing the manuscript.](#)

## References

- Andres, R., Marland, G., Boden, T., and Bischof, S.: Carbon dioxide emissions from fossil fuel consumption and cement manufacture, 1751-1991, and an estimate of their isotopic composition and latitudinal distribution, in: *The Carbon Cycle*, edited by Schimmel, D., pp. 53–62, 2000.
- 730 Andres, R., Boden, T., and Marland, G.: Monthly Fossil-Fuel CO<sub>2</sub> Emissions: Mass of Emissions Gridded by One Degree Latitude by One Degree Longitude - 2016, <https://doi.org/10.3334/CDIAC/FFE.MONTHLYMASS.2016>, 2009a.
- Andres, R., Boden, T., and Marland, G.: Monthly Fossil-Fuel CO<sub>2</sub> Emissions: Isomass of Emissions Gridded by One Degree Latitude by One Degree Longitude, <https://doi.org/10.3334/CDIAC/FFE.MONTHLYISOMASS.2016>, 2009b.
- 735 Andres, R., Boden, T., and Marland, G.: Annual Fossil-Fuel CO<sub>2</sub> Emissions: Global Stable Carbon Isotopic Signature, <https://doi.org/10.3334/CDIAC/FFE.DB1013.2017>, 2017.
- Bacastow, R. B., Keeling, C. D., and Whorf, T. P.: Seasonal amplitude increase in atmospheric CO<sub>2</sub> concentration at Mauna Loa, Hawaii, 1959-1982, *Journal of Geophysical Research: Atmospheres*, 90, 10 529–10 540, <https://doi.org/10.1029/JD090iD06p10529>, 1985.
- Ballantyne, A. P., Miller, J. B., and Tans, P. P.: Apparent seasonal cycle in isotopic discrimination of carbon in the atmosphere and biosphere due to vapor pressure deficit, *Global Biogeochemical Cycles*, 24, 1–16, <https://doi.org/10.1029/2009GB003623>, 2010.
- 740 Ballantyne, A. P., Miller, J. B., Baker, I. T., Tans, P. P., and White, J. W. C.: Novel applications of carbon isotopes in atmospheric CO<sub>2</sub>: what can atmospheric measurements teach us about processes in the biosphere?, *Biogeosciences*, 8, 3093–3106, <https://doi.org/10.5194/bg-8-3093-2011>, 2011.
- Barlow, J. M., Palmer, P. I., Bruhwiler, L. M., and Tans, P.: Analysis of CO<sub>2</sub> mole fraction data: First evidence of large-scale changes in CO<sub>2</sub> uptake at high northern latitudes, *Atmospheric Chemistry and Physics*, 15, 13 739–13 758, <https://doi.org/10.5194/acp-15-13739-2015>, 2015.
- 745 Bastos, A., Ciais, P., Chevallier, F., Rödenbeck, C., Ballantyne, A. P., Maignan, F., Yin, Y., Fernández-Martínez, M., Friedlingstein, P., Peñuelas, J., Piao, S. L., Sitch, S., Smith, W. K., Wang, X., Zhu, Z., Haverd, V., Kato, E., Jain, A. K., Lienert, S., Lombardozzi, D., Nabel, J. E., Peylin, P., Poulter, B., and Zhu, D.: Contrasting effects of CO<sub>2</sub> fertilization, land-use change and warming on seasonal amplitude of Northern Hemisphere CO<sub>2</sub> exchange, *Atmospheric Chemistry and Physics*, 19, 12 361–12 375, <https://doi.org/10.5194/acp-19-12361-2019>, 2019.
- 750 Battaglia, G. and Joos, F.: Marine N<sub>2</sub>O Emissions From Nitrification and Denitrification Constrained by Modern Observations and Projected in Multimillennial Global Warming Simulations, *Global Biogeochemical Cycles*, 32, 92–121, <https://doi.org/10.1002/2017GB005671>, 2018.
- 755 Battipaglia, G., Saurer, M., Cherubini, P., Calfapietra, C., McCarthy, H. R., Norby, R. J., and Francesca Cotrufo, M.: Elevated CO<sub>2</sub> increases tree-level intrinsic water use efficiency: insights from carbon and oxygen isotope analyses in tree rings across three forest FACE sites, *New Phytologist*, 197, 544–554, <https://doi.org/10.1111/nph.12044>, 2013.
- Becker, M., Steinhoff, T., and Körtzinger, A.: A Detailed View on the Seasonality of Stable Carbon Isotopes Across the North Atlantic, *Global Biogeochemical Cycles*, 32, 1406–1419, <https://doi.org/10.1029/2018GB005905>, 2018.
- 760 Botía, S., Komiya, S., Marshall, J., Koch, T., Gałkowski, M., Lavric, J., Gomes-Alves, E., Walter, D., Fisch, G., Pinho, D. M., Nelson, B. W., Martins, G., Lujikx, I. T., Koren, G., Florentie, L., Carioca de Araújo, A., Sá, M., Andreae, M. O., Heimann, M., Peters, W., and Gerbig, C.: The CO<sub>2</sub> record at the Amazon Tall Tower Observatory: A new opportunity to study processes on seasonal and inter-annual scales, *Global Change Biology*, 28, 588–611, <https://doi.org/10.1111/gcb.15905>, 2022.

- Bugmann, H. and Christof, B.: Will the CO<sub>2</sub> fertilization effect in forests be offset by reduced tree longevity?, *Oecologia*, 165, 533–544, 765 <https://doi.org/https://doi.org/10.1007/s00442-010-1837-4>, 2011.
- Campbell, J. E., Berry, J. A., Seibt, U., Smith, S. J., Montzka, S. A., Launois, T., Belviso, S., Bopp, L., and Laine, M.: Large historical growth in global terrestrial gross primary production, *Nature*, 544, 84–87, 2017.
- Castro-Morales, K., Schürmann, G., Köstler, C., Rödenbeck, C., Heimann, M., and Zaehle, S.: Three decades of simulated global terrestrial carbon fluxes from a data assimilation system confronted with different periods of observations, *Biogeosciences*, 16, 3009–3032, 770 <https://doi.org/10.5194/bg-16-3009-2019>, 2019.
- Cernusak, L. A. and Ubierna, N.: Carbon Isotope Effects in Relation to CO<sub>2</sub> Assimilation by Tree Canopies, pp. 291–310, Springer International Publishing, Cham, ISBN 978-3-030-92698-4, [https://doi.org/10.1007/978-3-030-92698-4\\_9](https://doi.org/10.1007/978-3-030-92698-4_9), 2022.
- Cernusak, L. A., Ubierna, N., Winter, K., Holtum, J. A. M., Marshall, J. D., and Farquhar, G. D.: Environmental and physiological determinants of carbon isotope discrimination in terrestrial plants, *New Phytologist*, 200, 950–965, 775 <https://doi.org/https://doi.org/10.1111/nph.12423>, 2013.
- Cooperative Global Atmospheric Data Integration Project: Multi-laboratory compilation of synchronized and gap-filled atmospheric carbon dioxide records for the period 1979–2012 (obspack\_co2\_1\_GLOBALVIEW-CO2\_2013\_v1.0.4\_2013-12-23), <https://doi.org/10.3334/OBSPACK/1002>, 2013.
- Craig, H.: Isotopic standards for carbon and oxygen and correction factors for mass-spectrometric analysis of carbon dioxide, *Geochimica et Cosmochimica Acta*, 12, 133–149, [https://doi.org/https://doi.org/10.1016/0016-7037\(57\)90024-8](https://doi.org/https://doi.org/10.1016/0016-7037(57)90024-8), 1957. 780
- Dargaville, R. J., Heimann, M., McGuire, A. D., Prentice, I. C., Kicklighter, D. W., Joos, F., Klein, J. S., Esser, G., Foley, J., Kaplan, J., Meier, R. A., Melillo, J. M., Moore, B., Ramankutty, N., Reichenau, T., Schloss, A., Sitch, S., Tian, H., Williams, L. J., and Wittenberg, U.: Evaluation of terrestrial carbon cycle models with atmospheric CO<sub>2</sub> measurements: Results from transient simulations considering increasing CO<sub>2</sub>, climate, and land-use effects, *Global Biogeochemical Cycles*, 16, <https://doi.org/10.1029/2001gb001426>, 2002.
- 785 Farquhar, G.: Carbon Isotope Discrimination And Photosynthesis, *Annual Review of Plant Physiology and Plant Molecular Biology*, 40, 503–537, <https://doi.org/10.1146/annurev.arplant.40.1.503>, 1989.
- Farquhar, G. and Cernusak, L.: Ternary effects on the gas exchange of isotopologues of carbon dioxide, *Plant, Cell and Environment*, 35, 1221–1231, <https://doi.org/10.1111/j.1365-3040.2012.02484.x>, 2012.
- Farquhar, G. D., O’Leary, M. H., and Berry, J. A.: On the relationship between carbon isotope discrimination and the intercellular carbon 790 dioxide concentration in leaves, *Aust. J. Plant Physiol.*, 9, 121–137, 1982.
- Fay, A. R., Gregor, L., Landschützer, P., McKinley, G. A., Gruber, N., Gehlen, M., Iida, Y., Laruelle, G. G., Rödenbeck, C., Roobaert, A., and Zeng, J.: SeaFlux: harmonization of air–sea CO<sub>2</sub> fluxes from surface *p*CO<sub>2</sub> data products using a standardized approach, *Earth System Science Data*, 13, 4693–4710, <https://doi.org/10.5194/essd-13-4693-2021>, 2021.
- Forkel, M., Carvalhais, N., Rödenbeck, C., Keeling, R., Heimann, M., Thonicke, K., Zaehle, S., and Reichstein, M.: Enhanced seasonal CO<sub>2</sub> 795 exchange caused by amplified plant productivity in northern ecosystems, *Science*, 351, 696–699, <https://doi.org/10.1126/science.aac4971>, 2016.
- Francey, R. J., Tans, P. P., Allison, C. E., Enting, I. G., White, J. W. C., and Trolrier, M.: Changes in oceanic and terrestrial carbon uptake since 1982, *Nature*, 373, 326–330, 1995.
- Frank, D. C., Poulter, B., Saurer, M., Esper, J., Huntingford, C., Helle, G., Treydte, K., Zimmermann, N. E., Schleser, G. H., Ahlstrom, 800 A., Ciais, P., Friedlingstein, P., Levis, S., Lomas, M., Sitch, S., Viovy, N., Andreu-Hayles, L., Bednarz, Z., Berninger, F., Boettger, T., D’Alessandro, C. M., Daux, V., Filot, M., Grabner, M., Gutierrez, E., Haupt, M., Hiltunen, E., Jungner, H., Kalela-Brundin, M., Krapiec,

- M., Leuenberger, M., Loader, N. J., Marah, H., Masson-Delmotte, V., Pazdur, A., Pawelczyk, S., Pierre, M., Planells, O., Pukiene, R., Reynolds-Henne, C. E., Rinne, K. T., Saracino, A., Sonninen, E., Stievenard, M., Switsur, V. R., Szczepanek, M., Szychowska-Krapiec, E., Todaro, L., Waterhouse, J. S., and Weigl, M.: Water-use efficiency and transpiration across European forests during the Anthropocene, *Nature Climate Change*, 5, 579–583, 2015.
- 805 Friedlingstein, P., O’Sullivan, M., Jones, M. W., Andrew, R. M., Hauck, J., Olsen, A., Peters, G. P., Peters, W., Pongratz, J., Sitch, S., Le Quéré, C., Canadell, J. G., Ciais, P., Jackson, R. B., Alin, S., Aragão, L. E., Arneeth, A., Arora, V., Bates, N. R., Becker, M., Benoit-Cattin, A., Bittig, H. C., Bopp, L., Bultan, S., Chandra, N., Chevallier, F., Chini, L. P., Evans, W., Florentie, L., Forster, P. M., Gasser, T., Gehlen, M., Gilfillan, D., Gkritzalis, T., Gregor, L., Gruber, N., Harris, I., Hartung, K., Haverd, V., Houghton, R. A., Ilyina, T., Jain, A. K., Joetzjer, E., Kadono, K., Kato, E., Kitidis, V., Korsbakken, J. I., Landschützer, P., Lefèvre, N., Lenton, A., Lienert, S., Liu, Z., Lombardozzi, D., Marland, G., Metzl, N., Munro, D. R., Nabel, J. E., Nakaoka, S. I., Niwa, Y., O’Brien, K., Ono, T., Palmer, P. I., Pierrot, D., Poulter, B., Resplandy, L., Robertson, E., Rödenbeck, C., Schwinger, J., Séférian, R., Skjelvan, I., Smith, A. J., Sutton, A. J., Tanhua, T., Tans, P. P., Tian, H., Tilbrook, B., Van Der Werf, G., Vuichard, N., Walker, A. P., Wanninkhof, R., Watson, A. J., Willis, D., Wiltshire, A. J., Yuan, W., Yue, X., and Zaehle, S.: Global Carbon Budget 2020, *Earth System Science Data*, 12, 3269–3340, <https://doi.org/10.5194/essd-12-3269-2020>, 2020.
- 810 GLOBALVIEW-CO2C13: Cooperative Atmospheric Data Integration Project - d13C of Carbon Dioxide, 2009.
- Gonsamo, A., D’Odorico, P., Chen, J. M., Wu, C., and Buchmann, N.: Changes in vegetation phenology are not reflected in atmospheric CO<sub>2</sub> and 13C/12C seasonality, *Global Change Biology*, 23, 4029–4044, <https://doi.org/10.1111/gcb.13646>, 2017.
- Graven, H. D., Keeling, R. F., Piper, S. C., Patra, P. K., Stephens, B. B., Wofsy, S. C., Welp, L. R., Sweeney, C., Tans, P. P., Kelley, J. J., Daube, B. C., Kort, E. A., Santoni, G. W., and Bent, J. D.: Enhanced Seasonal Exchange of CO<sub>2</sub> by Northern Ecosystems Since 1960, *Science*, 341, 1085–1089, <https://doi.org/10.1126/science.1239207>, 2013.
- 820 Graven, H. D., Warren, H., Gibbs, H. K., Khatiwala, S., Koven, C., Lester, J., Levin, I., Spawn-Lee, S. A., and Wieder, W.: Bomb radiocarbon evidence for strong global carbon uptake and turnover in terrestrial vegetation, *Science*, 384, 1335–1339, <https://doi.org/10.1126/science.adl4443>, 2024.
- 825 Gurney, K. R., Law, R. M., Denning, A. S., Rayner, P. J., Pak, B. C., Baker, D., Bousquet, P., Bruhwiler, L., Chen, Y.-H., Ciais, P., Fung, I. Y., Heimann, M., John, J., Maki, T., Maksyutov, S., Peylin, P., Prather, M., and Taguchi, S.: Transcom 3 inversion inter-comparison: Model mean results for the estimation of seasonal carbon sources and sinks, *Global Biogeochemical Cycles*, 18, <https://doi.org/https://doi.org/10.1029/2003GB002111>, 2004.
- Harris, I., Osborn, T. J., Jones, P., and Lister, D.: Version 4 of the CRU TS monthly high-resolution gridded multivariate climate dataset, *Scientific Data*, 7, 1–18, <https://doi.org/10.1038/s41597-020-0453-3>, 2020.
- 830 Hauck, J. and Völker, C.: Rising atmospheric CO<sub>2</sub> leads to large impact of biology on Southern Ocean CO<sub>2</sub> uptake via changes of the Revelle factor, *Geophysical Research Letters*, 42, 1459–1464, <https://doi.org/10.1002/2015GL063070>, 2015.
- Heimann, M. and Körner, S.: The Global Atmospheric Tracer Model TM3, Tech. rep., Max-Planck-Institut für Biogeochemie, Max-Planck-Institut für Biogeochemie, Jena (Germany), 2003.
- 835 Heimann, M., Keeling, C. D., and Tucker, C. J.: A three dimensional model of atmospheric CO<sub>2</sub> transport based on observed winds: 3. Seasonal cycle and synoptic time scale variations, in: *Aspects of Climate Variability in the Pacific and the Western Americas*, pp. 277–303, American Geophysical Union (AGU), ISBN 9781118664285, <https://doi.org/10.1029/GM055p0277>, 1989.
- Heimann, M., Esser, G., Haxeltine, A., Kaduk, J., Kicklighter, D. W., Knorr, W., Kohlmaier, G. H., McGuire, A. D., Melillo, J., Moore, B., Otto, R. D., Prentice, I. C., Sauf, W., Schloss, A., Sitch, S., Wittenberg, U., and Würth, G.: Evaluation of terrestrial carbon cycle models



- 840 through simulations of the seasonal cycle of atmospheric CO<sub>2</sub>: First results of a model intercomparison study, *Global Biogeochemical Cycles*, 12, 1–24, <https://doi.org/10.1029/97GB01936>, 1998.
- Hurtt, G. C., Chini, L., Sahajpal, R., Frolking, S., Bodirsky, B. L., Calvin, K., Doelman, J. C., Fisk, J., Fujimori, S., Goldewijk, K. K., Hasegawa, T., Havlik, P., Heinemann, A., Humpenöder, F., Jungclaus, J., Kaplan, J. O., Kennedy, J., Krisztin, T., Lawrence, D., Lawrence, P., Ma, L., Mertz, O., Pongratz, J., Popp, A., Poulter, B., Riahi, K., Shevliakova, E., Stehfest, E., Thornton, P., Tubiello, F. N., van Vuuren, D. P., and Zhang, X.: Harmonization of global land use change and management for the period 850–2100 (LUH2) for CMIP6, *Geoscientific Model Development*, 13, 5425–5464, <https://doi.org/10.5194/gmd-13-5425-2020>, 2020.
- 845 Ito, A., Inatomi, M., Huntzinger, D. N., Schwalm, C., Michalak, A. M., Cook, R., King, A. W., Mao, J., Wei, Y., Post, W. M., Wang, W., Arain, M. A., Huang, S., Hayes, D. J., Ricciuto, D. M., Shi, X., Huang, M., Lei, H., Tian, H., Lu, C., Yang, J., Tao, B., Jain, A., Poulter, B., Peng, S., Ciais, P., Fisher, J. B., Parazoo, N., Schaefer, K., Peng, C., Zeng, N., and Zhao, F.: Decadal trends in the seasonal-cycle amplitude of terrestrial CO<sub>2</sub> exchange resulting from the ensemble of terrestrial biosphere models, *Tellus B: Chemical and Physical Meteorology*, 68, 28 968, <https://doi.org/10.3402/tellusb.v68.28968>, 2016.
- 850 Jeltsch-Thömmes, A. and Joos, F.: Modeling the evolution of pulse-like perturbations in atmospheric carbon and carbon isotopes: The role of weathering-sedimentation imbalances, *Climate of the Past*, 16, 423–451, <https://doi.org/10.5194/cp-16-423-2020>, 2020.
- Jeltsch-Thömmes, A. and Joos, F.: Carbon Cycle Responses to Changes in Weathering and the Long-Term Fate of Stable Carbon Isotopes, *Paleoceanography and Paleoclimatology*, 38, e2022PA004 577, <https://doi.org/https://doi.org/10.1029/2022PA004577>, e2022PA004577 2022PA004577, 2023.
- 855 Jin, Y., Keeling, R. F., Stephens, B. B., Long, M. C., Patra, P. K., Rödenbeck, C., Morgan, E. J., Kort, E. A., and Sweeney, C.: Improved atmospheric constraints on Southern Ocean CO<sub>2</sub> exchange, *Proceedings of the National Academy of Sciences*, 121, e2309333 121, <https://doi.org/10.1073/pnas.2309333121>, 2024.
- 860 Joos, F. and Bruno, M.: Long-term variability of the terrestrial and oceanic carbon sinks and the budgets of the carbon isotopes <sup>13</sup>C and <sup>14</sup>C, *Global Biogeochemical Cycles*, 12, 277–295, <https://doi.org/https://doi.org/10.1029/98GB00746>, 1998.
- Joos, F., Hameau, A., Frölicher, T. L., and Stephenson, D. B.: Anthropogenic Attribution of the Increasing Seasonal Amplitude in Surface Ocean pCO<sub>2</sub>, *Geophysical Research Letters*, 50, e2023GL102 857, <https://doi.org/https://doi.org/10.1029/2023GL102857>, e2023GL102857 2023GL102857, 2023.
- 865 Kalnay, E., Kanamitsu, M., Kistler, R., Collins, W., Deaven, D., Gandin, L., Iredell, M., Saha, S., White, G., Woollen, J., Zhu, Y., Leetmaa, A., Reynolds, R., Chelliah, M., Ebisuzaki, W., Higgins, W., Janowiak, J., Mo, K. C., Ropelewski, C., Wang, J., Jenne, R., and Joseph, D.: The NCEP/NCAR 40-Year Reanalysis Project, *Bulletin of the American Meteorological Society*, 77, 437–471, [https://doi.org/10.1175/1520-0477\(1996\)077<0437:TNYRP>2.0.CO;2](https://doi.org/10.1175/1520-0477(1996)077<0437:TNYRP>2.0.CO;2), 1996.
- Kaminski, T., Heimann, M., and Giering, R.: A Global Scale Inversion of the Transport of CO<sub>2</sub> Based on a Matrix Representation of an Atmospheric Transport Model Derived by Its Adjoint, in: *Air Pollution Modeling and Its Application XII*, pp. 247–255, Springer US, Boston, MA, [https://doi.org/10.1007/978-1-4757-9128-0\\_26](https://doi.org/10.1007/978-1-4757-9128-0_26), 1998.
- 870 Kauwe, M. G., Medlyn, B. E., Zaehle, S., Walker, A. P., Dietze, M. C., Hickler, T., Jain, A. K., Luo, Y., Parton, W. J., Prentice, I. C., Smith, B., Thornton, P. E., Wang, S., Wang, Y.-P., Wårlind, D., Weng, E., Crous, K. Y., Ellsworth, D. S., Hanson, P. J., Kim, H.-S., Warren, J. M., Oren, R., and Norby, R. J.: Forest water use and water use efficiency at elevated CO<sub>2</sub>: a model-data intercomparison at two contrasting temperate forest FACE sites, *Global Change Biology*, 19, 1759–1779, <https://doi.org/10.1111/gcb.12164>, 2013.
- 875 Keeling, C. D.: The Concentration and Isotopic Abundances of Carbon Dioxide in the Atmosphere, *Tellus*, 12, 200–203, <https://doi.org/https://doi.org/10.1111/j.2153-3490.1960.tb01300.x>, 1960.

- Keeling, C. D., Carter, A. F., and Mook, W. G.: Seasonal, latitudinal, and secular variations in the abundance and isotopic ratios of atmospheric CO<sub>2</sub>: 2. Results from oceanographic cruises in the tropical Pacific Ocean, *Journal of Geophysical Research: Atmospheres*, 89, 4615–4628, <https://doi.org/https://doi.org/10.1029/JD089iD03p04615>, 1984.
- 880 Keeling, C. D., Bacastow, R. B., Carter, A. F., Piper, S. C., Whorf, T. P., Heimann, M., Mook, W. G., and Roeloffzen, H.: A three dimensional model of atmospheric CO<sub>2</sub> transport based on observed winds: 1. Analysis of Observational Data, in: *Aspects of Climate Variability in the Pacific and the Western Americas*, pp. 165–236, American Geophysical Union (AGU), ISBN 9781118664285, <https://doi.org/10.1029/GM055p0165>, 1989.
- 885 Keeling, C. D., Chin, J. F. S., and Whorf, T. P.: Increased activity of northern vegetation inferred from atmospheric CO<sub>2</sub> measurements, *Nature*, 382, 146–149, <https://doi.org/10.1038/382146a0>, 1996.
- Keeling, C. D., Piper, S. C., Bacastow, R. B., Wahlen, M., Whorf, T. P., Heimann, M., and Meijer, H. A.: Exchanges of atmospheric CO<sub>2</sub> and <sup>13</sup>CO<sub>2</sub> with the terrestrial biosphere and oceans from 1978 to 2000. I. Global aspects, SIO Reference Series, No. 01-06, Scripps Institution of Oceanography, San Diego, p. 88, 2001.
- 890 Keeling, C. D., Piper, S. C., Bacastow, R. B., Wahlen, M., Whorf, T. P., Heimann, M., and Meijer, H. A.: Atmospheric CO<sub>2</sub> and <sup>13</sup>CO<sub>2</sub> Exchange with the Terrestrial Biosphere and Oceans from 1978 to 2000: Observations and Carbon Cycle Implications, in: *A History of Atmospheric CO<sub>2</sub> and Its Effects on Plants, Animals, and Ecosystems*, edited by Baldwin, I. T., Caldwell, M. M., Heldmaier, G., Jackson, R. B., Lange, O. L., Mooney, H. A., Schulze, E.-D., Sommer, U., Ehleringer, J. R., Denise Dearing, M., and Cerling, T. E., pp. 83–113, Springer New York, New York, NY, ISBN 978-0-387-27048-7, [https://doi.org/10.1007/0-387-27048-5\\_5](https://doi.org/10.1007/0-387-27048-5_5), 2005.
- 895 Keeling, R. F., Graven, H. D., Welp, L. R., Resplandy, L., Bi, J., Piper, S. C., Sun, Y., Bollenbacher, A., and Meijer, H. A. J.: Atmospheric evidence for a global secular increase in carbon isotopic discrimination of land photosynthesis, *Proceedings of the National Academy of Sciences*, 114, 10361–10366, <https://doi.org/10.1073/pnas.1619240114>, 2017.
- Keenan, T. F., Hollinger, D. Y., Bohrer, G., Dragoni, D., Munger, J. W., Schmid, H. P., and Richardson, A. D.: Increase in forest water-use efficiency as atmospheric carbon dioxide concentrations rise, *Nature*, 499, 324–327, <https://doi.org/10.1038/nature12291>, 2013.
- 900 Keller, K. M., Joos, F., and Raible, C. C.: Time of emergence of trends in ocean biogeochemistry, *Biogeosciences*, 11, 3647–3659, <https://doi.org/10.5194/bg-11-3647-2014>, 2014.
- Keller, K. M., Lienert, S., Bozbiyik, A., Stocker, T. F., Churakova (Sidorova), O. V., Frank, D. C., Klesse, S., Koven, C. D., Leuenberger, M., Riley, W. J., Saurer, M., Siegwolf, R., Weigt, R. B., and Joos, F.: 20th century changes in carbon isotopes and water-use efficiency: tree-ring-based evaluation of the CLM4.5 and LPX-Bern models, *Biogeosciences*, 14, 2641–2673, <https://doi.org/10.5194/bg-14-2641-2017>,
- 905 2017.
- Knauer, J., Zaehle, S., Reichstein, M., Medlyn, B. E., Forkel, M., Hagemann, S., and Werner, C.: The response of ecosystem water-use efficiency to rising atmospheric CO<sub>2</sub> concentrations: sensitivity and large-scale biogeochemical implications, *New Phytologist*, 213, 1654–1666, <https://doi.org/https://doi.org/10.1111/nph.14288>, 2017.
- Körner, C.: A matter of tree longevity, *Science*, 355, 130–131, <https://doi.org/10.1126/science.aal2449>, 2017.
- 910 Landschützer, P., Gruber, N., Bakker, D. C. E., and Schuster, U.: Recent variability of the global ocean carbon sink, *Global Biogeochemical Cycles*, 28, 927–949, <https://doi.org/10.1002/2014GB004853>, 2014.
- Lienert, S. and Joos, F.: A Bayesian ensemble data assimilation to constrain model parameters and land-use carbon emissions, *Biogeosciences*, 15, 2909–2930, <https://doi.org/10.5194/bg-15-2909-2018>, 2018.
- Lloyd, J. and Farquhar, G.: C<sup>13</sup> discrimination during CO<sub>2</sub> assimilation by the terrestrial biosphere, *Oecologia*, 99, 201–215, <https://doi.org/10.1007/BF00627732>, 1994.
- 915

- Long, M. C., Stephens, B. B., McKain, K., Sweeney, C., Keeling, R. F., Kort, E. A., Morgan, E. J., Bent, J. D., Chandra, N., Chevallier, F., Commane, R., Daube, B. C., Krummel, P. B., Loh, Z., Lujikx, I. T., Munro, D., Patra, P., Peters, W., Ramonet, M., Rödenbeck, C., Stavert, A., Tans, P., and Wofsy, S. C.: Strong Southern Ocean carbon uptake evident in airborne observations, *Science*, 374, 1275–1280, <https://doi.org/10.1126/science.abi4355>, 2021.
- 920 Lueker, T., Keeling, R., Bollenbacher, A., Walker, S., Morgan, E., and Brooks, M.: Calibration Methodology for the Scripps 13C/12C and 18O/16O stable Isotope program 1992-2018, UC San Diego: Scripps Institution of Oceanography. Retrieved from <https://escholarship.org/uc/item/4n93p288>, p. 39, 2020.
- Majkut, J. D., Carter, B. R., Frölicher, T. L., Dufour, C. O., Rodgers, K. B., and Sarmiento, J. L.: An observing system simulation for Southern Ocean carbon dioxide uptake, *Philosophical Transactions of the Royal Society A: Mathematical, Physical and Engineering Sciences*, 372, 20130 046, <https://doi.org/10.1098/rsta.2013.0046>, 2014.
- 925 Masarie, K. A., Peters, W., Jacobson, A. R., and Tans, P. P.: ObsPack: a framework for the preparation, delivery, and attribution of atmospheric greenhouse gas measurements, *Earth System Science Data*, 6, 375–384, <https://doi.org/10.5194/essd-6-375-2014>, 2014.
- Menviel, L., Mouchet, A., Meissner, K. J., Joos, F., and England, M. H.: Impact of oceanic circulation changes on atmospheric  $\delta^{13}\text{C}_{\text{CO}_2}$ , *Global Biogeochemical Cycles*, 29, 1944–1961, <https://doi.org/10.1002/2015GB005207>, 2015.
- 930 Mook, W.: 13C in atmospheric CO<sub>2</sub>, *Netherlands Journal of Sea Research*, 20, 211–223, [https://doi.org/10.1016/0077-7579\(86\)90043-8](https://doi.org/10.1016/0077-7579(86)90043-8), 1986.
- Peng, S., Ciais, P., Chevallier, F., Peylin, P., Cadule, P., Sitch, S., Piao, S., Ahlström, A., Huntingford, C., Levy, P., Li, X., Liu, Y., Lomas, M., Poulter, B., Viovy, N., Wang, T., Wang, X., Zaehle, S., Zeng, N., Zhao, F., and Zhao, H.: Benchmarking the seasonal cycle of CO<sub>2</sub> fluxes simulated by terrestrial ecosystem models, *Global Biogeochemical Cycles*, 29, 46–64, <https://doi.org/10.1002/2014GB004931>, 2015.
- 935 Peylin, P., Law, R. M., Gurney, K. R., Chevallier, F., Jacobson, A. R., Maki, T., Niwa, Y., Patra, P. K., Peters, W., Rayner, P. J., Rödenbeck, C., Van Der Laan-Luijkx, I. T., and Zhang, X.: Global atmospheric carbon budget: Results from an ensemble of atmospheric CO<sub>2</sub> inversions, *Biogeosciences*, 10, 6699–6720, <https://doi.org/10.5194/bg-10-6699-2013>, 2013.
- Peylin, P., Bacour, C., MacBean, N., Leonard, S., Rayner, P., Kuppel, S., Koffi, E., Kane, A., Maignan, F., Chevallier, F., Ciais, P., and Prunet, P.: A new stepwise carbon cycle data assimilation system using multiple data streams to constrain the simulated land surface carbon cycle, *Geoscientific Model Development*, 9, 3321–3346, <https://doi.org/10.5194/gmd-9-3321-2016>, 2016.
- 940 Peñuelas, J., Canadell, J. G., and Ogaya, R.: Increased water-use efficiency during the 20th century did not translate into enhanced tree growth, *Global Ecology and Biogeography*, 20, 597–608, <https://doi.org/10.1111/j.1466-8238.2010.00608.x>, 2011.
- Piao, S., Liu, Z., Wang, Y., Ciais, P., Yao, Y., Peng, S., Chevallier, F., Friedlingstein, P., Janssens, I. A., Peñuelas, J., Sitch, S., and Wang, T.: On the causes of trends in the seasonal amplitude of atmospheric CO<sub>2</sub>, *Global Change Biology*, 24, 608–616, <https://doi.org/10.1111/gcb.13909>, 2018.
- 945 Quay, P. D., Sonnerup, R., Munro, D. R., and Sweeney, C.: Anthropogenic CO<sub>2</sub> accumulation and uptake rates in the Pacific Ocean based on changes in the 13 C/ 12 C of dissolved inorganic carbon, *Global Biogeochemical Cycles*, 31, 59–80, <https://doi.org/10.1002/2016GB005460>, 2017.
- Ritz, S. P., Stocker, T. F., Joos, F., Ritz, S. P., Stocker, T. F., and Joos, F.: A Coupled Dynamical Ocean–Energy Balance Atmosphere Model for Paleoclimate Studies, *Journal of Climate*, 24, 349–375, <https://doi.org/10.1175/2010JCLI3351.1>, 2011.
- 950 Saurer, M. and Voelker, S.: Intrinsic Water-Use Efficiency Derived from Stable Carbon Isotopes of Tree-Rings, pp. 481–498, Springer International Publishing, Cham, ISBN 978-3-030-92698-4, [https://doi.org/10.1007/978-3-030-92698-4\\_17](https://doi.org/10.1007/978-3-030-92698-4_17), 2022.

- Saurer, M., Spahni, R., Frank, D. C., Joos, F., Leuenberger, M., Loader, N. J., McCarroll, D., Gagen, M., Poulter, B., Siegwolf, R. T., Andreu-Hayles, L., Boettger, T., Dorado Liñán, I., Fairchild, I. J., Friedrich, M., Gutierrez, E., Haupt, M., Hiltunen, E., Heinrich, I., Helle, G., Grudd, H., Jalkanen, R., Levanič, T., Linderholm, H. W., Robertson, I., Sonninen, E., Treydte, K., Waterhouse, J. S., Woodley, E. J., Wynn, P. M., and Young, G. H.: Spatial variability and temporal trends in water-use efficiency of European forests, *Global Change Biology*, 20, 3700–3712, <https://doi.org/10.1111/gcb.12717>, 2014.
- Scholz, M., Kaplan, J. O., Knorr, W., and Heimann, M.: Climate and interannual variability of the atmosphere-biosphere  $^{13}\text{C}$  flux, *Geophysical Research Letters*, 30, 1–4, <https://doi.org/10.1029/2002GL015631>, 2003.
- Scholz, M., Ciais, P., and Heimann, M.: Modeling terrestrial  $^{13}\text{C}$  cycling: Climate, land use and fire, *Global Biogeochemical Cycles*, 22, 1–13, <https://doi.org/10.1029/2006GB002899>, 2008.
- Schürmann, G. J., Kaminski, T., Köstler, C., Carvalhais, N., Voßbeck, M., Kattge, J., Giering, R., Rödenbeck, C., Heimann, M., and Zaehle, S.: Constraining a land-surface model with multiple observations by application of the MPI-Carbon Cycle Data Assimilation System V1.0, *Geoscientific Model Development*, 9, 2999–3026, <https://doi.org/10.5194/gmd-9-2999-2016>, 2016.
- Sitch, S., Smith, B., Prentice, I. C., Arneth, A., Bondeau, A., Cramer, W., Kaplan, J. O., Levis, S., Lucht, W., Sykes, M. T., Thonicke, K., and Venevsky, S.: Evaluation of ecosystem dynamics, plant geography and terrestrial carbon cycling in the LPJ dynamic global vegetation model, *Global Change Biology*, 9, 161–185, <https://doi.org/https://doi.org/10.1046/j.1365-2486.2003.00569.x>, 2003.
- Still, C. J., Berry, J. A., Collatz, G. J., and DeFries, R. S.: Global distribution of  $\text{C}_3$  and  $\text{C}_4$  vegetation: Carbon cycle implications, *Global Biogeochemical Cycles*, 17, 6–1–6–14, <https://doi.org/https://doi.org/10.1029/2001GB001807>, 2003.
- Stocker, B. D., Spahni, R., and Joos, F.: DYPTOP: a cost-efficient TOPMODEL implementation to simulate sub-grid spatio-temporal dynamics of global wetlands and peatlands, *Geoscientific Model Development*, 7, 3089–3110, <https://doi.org/10.5194/gmd-7-3089-2014>, 2014.
- Strassmann, K. M., Joos, F., and Fischer, G.: Simulating effects of land use changes on carbon fluxes: past contributions to atmospheric  $\text{CO}_2$  increases and future commitments due to losses of terrestrial sink capacity, *Tellus B*, 60, 583–603, 2008.
- Takahashi, T., Sutherland, S. C., Wanninkhof, R., Sweeney, C., Feely, R. A., Chipman, D. W., Hales, B., Friederich, G., Chavez, F., Sabine, C., Watson, A., Bakker, D. C., Schuster, U., Metzl, N., Yoshikawa-Inoue, H., Ishii, M., Midorikawa, T., Nojiri, Y., Körtzinger, A., Steinhoff, T., Hoppema, M., Olafsson, J., Arnarson, T. S., Tilbrook, B., Johannessen, T., Olsen, A., Bellerby, R., Wong, C., Delille, B., Bates, N., and de Baar, H. J.: Climatological mean and decadal change in surface ocean  $\text{pCO}_2$ , and net sea–air  $\text{CO}_2$  flux over the global oceans, *Deep Sea Research Part II: Topical Studies in Oceanography*, 56, 554–577, <https://doi.org/10.1016/j.dsr2.2008.12.009>, 2009.
- Tans, P. P., Berry, J. A., and Keeling, R. F.: Oceanic  $^{13}\text{C}/^{12}\text{C}$  observations: A new window on ocean  $\text{CO}_2$  uptake, *Global Biogeochemical Cycles*, 7, 353–368, <https://doi.org/https://doi.org/10.1029/93GB00053>, 1993.
- Tian, H., Yang, J., Lu, C., Xu, R., Canadell, J. G., Jackson, R. B., Arneth, A., Chang, J., Chen, G., Ciais, P., Gerber, S., Ito, A., Huang, Y., Joos, F., Lienert, S., Messina, P., Olin, S., Pan, S., Peng, C., Saikawa, E., Thompson, R. L., Vuichard, N., Winiwarter, W., Zaehle, S., Zhang, B., Zhang, K., and Zhu, Q.: The Global  $\text{N}_2\text{O}$  Model Intercomparison Project, *Bulletin of the American Meteorological Society*, 99, 1231–1251, <https://doi.org/10.1175/BAMS-D-17-0212.1>, 2018.
- Trudinger, C. M., Enting, I. G., Rayner, P. J., and Francey, R. J.: Kalman filter analysis of ice core data 2. Double deconvolution of  $\text{CO}_2$  and  $\delta^{13}\text{C}$  measurements, *Journal of Geophysical Research: Atmospheres*, 107, ACH 5–1–ACH 5–24, <https://doi.org/https://doi.org/10.1029/2001JD001112>, 2002.

- van der Velde, I. R., Miller, J. B., Schaefer, K., Masarie, K. A., Denning, S., White, J. W. C., Tans, P. P., Krol, M. C., and Peters, W.:  
990 Biosphere model simulations of interannual variability in terrestrial  $^{13}\text{C}/^{12}\text{C}$  exchange, *Global Biogeochemical Cycles*, 27, 637–649,  
<https://doi.org/https://doi.org/10.1002/gbc.20048>, 2013.
- van der Velde, I. R., Miller, J. B., van der Molen, M. K., Tans, P. P., Vaughn, B. H., White, J. W. C., Schaefer, K., and Peters, W.: The  
CarbonTracker Data Assimilation System for  $\text{CO}_2$  and  $\delta^{13}\text{C}$  (CTDAS-C13 v1.0): retrieving information on land–atmosphere exchange  
processes, *Geoscientific Model Development*, 11, 283–304, <https://doi.org/10.5194/gmd-11-283-2018>, 2018.
- 995 Voelker, S. L., Brooks, J. R., Meinzer, F. C., Anderson, R., Bader, M. K.-F., Battipaglia, G., Becklin, K. M., Beerling, D., Bert, D., Betancourt,  
J. L., Dawson, T. E., Domec, J.-C., Guyette, R. P., Körner, C., Leavitt, S. W., Linder, S., Marshall, J. D., Mildner, M., Ogée, J., Panyushkina,  
I., Plumpton, H. J., Pregitzer, K. S., Saurer, M., Smith, A. R., Siegwolf, R. T. W., Stambaugh, M. C., Talhelm, A. F., Tardif, J. C.,  
Van de Water, P. K., Ward, J. K., and Wingate, L.: A dynamic leaf gas-exchange strategy is conserved in woody plants under changing  
ambient  $\text{CO}_2$ : evidence from carbon isotope discrimination in paleo and  $\text{CO}_2$  enrichment studies, *Global Change Biology*, 22, 889–902,  
1000 <https://doi.org/10.1111/gcb.13102>, 2016.
- Walker, A. P., De Kauwe, M. G., Bastos, A., Belmecheri, S., Georgiou, K., Keeling, R. F., McMahon, S. M., Medlyn, B. E., Moore, D. J.,  
Norby, R. J., Zaehle, S., Anderson-Teixeira, K. J., Battipaglia, G., Brienen, R. J., Cabugao, K. G., Cailleret, M., Campbell, E., Canadell,  
J. G., Ciais, P., Craig, M. E., Ellsworth, D. S., Farquhar, G. D., Fatichi, S., Fisher, J. B., Frank, D. C., Graven, H., Gu, L., Haverd,  
V., Heilman, K., Heimann, M., Hungate, B. A., Iversen, C. M., Joos, F., Jiang, M., Keenan, T. F., Knauer, J., Körner, C., Leshyk, V. O.,  
1005 Leuzinger, S., Liu, Y., MacBean, N., Malhi, Y., McVicar, T. R., Penuelas, J., Pongratz, J., Powell, A. S., Riutta, T., Sabot, M. E., Schleucher,  
J., Sitch, S., Smith, W. K., Sulman, B., Taylor, B., Terrer, C., Torn, M. S., Treseder, K. K., Trugman, A. T., Trumbore, S. E., van Mantgem,  
P. J., Voelker, S. L., Whelan, M. E., and Zuidema, P. A.: Integrating the evidence for a terrestrial carbon sink caused by increasing  
atmospheric  $\text{CO}_2$ , *New Phytologist*, 229, 2413–2445, <https://doi.org/10.1111/nph.16866>, 2021.
- Wang, S., Zhang, Y., Ju, W., Chen, J. M., Ciais, P., Cescatti, A., Sardans, J., Janssens, I. A., Wu, M., Berry, J. A., Campbell, E., Fernández-  
1010 Martínez, M., Alkama, R., Sitch, S., Friedlingstein, P., Smith, W. K., Yuan, W., He, W., Lombardozzi, D., Kautz, M., Zhu, D., Lienert,  
S., Kato, E., Poulter, B., Sanders, T. G. M., Krüger, I., Wang, R., Zeng, N., Tian, H., Vuichard, N., Jain, A. K., Wiltshire, A., Haverd, V.,  
Goll, D. S., and Peñuelas, J.: Recent global decline of  $\text{CO}_2$  fertilization effects on vegetation photosynthesis, *Science*, 370, 1295–1300,  
<https://doi.org/10.1126/science.abb7772>, 2020.
- Wania, R., Ross, I., and Prentice, I. C.: Integrating peatlands and permafrost into a dynamic global vegetation model: 1. Evaluation and sensi-  
1015 tivity of physical land surface processes, *Global Biogeochemical Cycles*, 23, 1–19, <https://doi.org/https://doi.org/10.1029/2008GB003412>,  
2009a.
- Wania, R., Ross, I., and Prentice, I. C.: Integrating peatlands and permafrost into a dynamic global vegetation model:  
2. Evaluation and sensitivity of vegetation and carbon cycle processes, *Global Biogeochemical Cycles*, 23, 1–15,  
<https://doi.org/https://doi.org/10.1029/2008GB003413>, 2009b.
- 1020 Welch, B. L.: The Generalization of ‘Student’s’ Problem when Several Different Population Variances are Involved, *Biometrika*, 34, 28–35,  
<https://doi.org/10.2307/2332510>, 1947.
- Xu-Ri and Prentice, I. C.: Terrestrial nitrogen cycle simulation with a dynamic global vegetation model, *Global Change Biology*, 14, 1745–  
1764, <https://doi.org/https://doi.org/10.1111/j.1365-2486.2008.01625.x>, 2008.